WILEY

Prehistoric chamber tombs or geological pitfall? A multimethod case study from Ancient Aigeira with a focus on seismic full-waveform inversion

Katharina Rusch[1] [iD] | Daniel Köhn[1] | Harald Stümpel[1] | Walter Gauß[2] | Wolfgang Rabbel[1]

[1]Applied Geophysics, Institute of Geosciences, Kiel University, Kiel, Germany

[2]Austria Academy of Sciences, Austrian Archaeological Institute, Athens, Greece

Correspondence
Katharina Rusch, Applied Geophysics, Institute of Geosciences, Kiel University, Kiel, Schleswig-Holstein 24118, Germany.
Email: katharina.rusch@ifg.uni-kiel.de

Abstract

We show an extensive multimethod geophysical study of focusing on some enigmatic subsurface structures found at Ancient Aigeira (N Peloponnes, Greece) that could be interpreted either as prehistoric chamber tombs or complex weathering patterns of the local marl–conglomerate rock sequences. It turns out that the non-seismic methods do not allow to distinguish between an archaeological and a geological origin of the observed patterns with certainty. In contrast, we demonstrate how shear-wave seismics and full-waveform inversion (FWI) can be used in archaeological prospection for distinguishing between these alternative essentially different interpretational models that are not distinguishable through nonseismic prospection data. The example site Aigeira is strategically well located on a hill on the Northern Peloponnese overlooking the Corinthian Gulf and has been inhabited with occupational gaps since Middle Neolithic times until the 12th to early 14th century CE. Magnetics, ground-penetrating radar (GPR) and electrical resistivity tomography (ERT) reveal a honeycomb-shaped anomaly pattern that could have been interpreted as a system of prehistoric chamber tombs. The time-domain SH-FWI strategy based on a sequential inversion of low-pass and band-pass filtered data results in subsurface models for shear-wave velocity and density that accurately fits the complicated seismic data set. A highly heterogeneous subsurface is revealed that is characterized by linear cracks on a decimetre scale. The seismic FWI results are compared in detail with GPR, ERT and among each other. It turns out that the FWI result is consistent with each of these other geophysical methods but provides a more comprehensive subsurface characterization that it is supported by corings in addition. With the help of the seismic survey, we can reject the interpretation hypothesis of a prehistoric cemetery with chamber tombs and confirm that the enigmatic geophysical patterns represent a geological weathering structure that could be addressed as a reincised fan delta draped by reddish palaeosols.

1 | INTRODUCTION

In some geological situations, archaeological targets may be difficult, if not impossible, to identify through geophysical measurements. This is typically the case for sites where the archaeology and geological background do not show sufficient contrast. It applies, too, to targets where the cultural remains are not characterized by specific geometric structures like houses or streets but resemble geological structure. This difficulty of distinguishing between anthropogenic and natural subsurface is connected with targets from the Neolithic or Bronze Ages.

In these cases, a frequently conducted first step is broadening the spectrum of applied prospection methods providing other, possibly indicative, physical subsurface parameters, for example complementing standard magnetic mapping by ground-penetrating radar (GPR; e.g., Davis & Annan, 1989; Trinks et al., 2018; Wilken et al., 2015) or electrical resistivity tomography (ERT; e.g., Loke & Barker, 1995; Papadopoulos et al., 2007; Sporn et al., 2017; Wunderlich et al., 2018), which have often been successful in identifying cultural heritage in the subsurface.

However, in the case of a highly heterogeneous geology, it can still turn out to be impossible to distinguish between geological features and archaeological structures on the basis of magnetics, ERT and GPR alone. The subject of the present study is an example highlighting this situation. It is the case of a structure whose magnetic, electric resistivity and GPR reflection patters show high similarity with prehistoric chamber tombs. But this structure occurs in an area consisting of weathered conglomerate showing similar blocky cross sections. The structure was found in a previous survey by Rusch et al. (2020). In this case, the general low magnetic contrasts of archaeological and geological materials had motivated the additional application of GPR and ERT which had been applied successfully in the particular geological setting of Aigeira beforehand. However, in this case, no further progress could be achieved because the observed material parameter contrasts remained ambiguous with respect to the possible alternative targets (see Section 3).

In situations like these, imaging subsurface structure in terms of shear-wave velocity and density can be helpful because these material parameters are usually not correlated with magnetization and electric resistivity or dielectric permittivity. Indeed, the use of different sorts of seismic methods has proven to provide key information for a thorough interpretation in a number of case studies (e.g., Mecking et al., 2020; Polymenakos & Tweeton, 2017; Rabbel et al., 2004; Vafidis et al., 2003; Woelz et al., 2009). However, in the present case of potential near-surface prehistoric tombs, a particular problem rises from the required spatial resolution, which is of the order of a few 10 cm only and which is usually not achievable with conventional seismic imaging approaches.

Here, a more recent tool for the analysis of seismic data can provide a solution, the full-waveform inversion (FWI). Dokter et al. (2017) and Köhn et al. (2019) have shown that by using the whole waveform of the seismic data, the resolution can be increased to its wave-theoretical limit which allows the imaging of near-surface objects smaller than the seismic wavelength. Although the theoretical base of FWI was established as early as the 1980s (e.g., Virieux & Operto, 2009), first successful applications were published rather recently (e.g., Alam, 2019; Athanasopoulos & Bohlen, 2017; Tran et al., 2013). Many studies focus on methodological aspects using synthetic data, but the number of publication of studies using field data is increasing only slowly, especially studies not only limited to body waves but also incorporating surface waves (Dokter et al., 2017; Krampe et al., 2019). Only recently, first examples of FWI in an archaeological context were presented. Dokter et al. (2017) introduced a FWI approach to resolve the near-surface subsurface using SH/Love wave. Köhn et al. (2019) studied different SH-FWI strategies to improve the resolution of medieval canal structures. Schwardt et al. (2020) were able to relate SH-FWI results to lithological properties of soils.

In this study, we investigate the applicability of a combined GPR and FWI approach to map potential chamber tombs in Ancient Aigeira. This high-resolution imaging approach is able to resolve complex anomaly patterns on the decimetre scale, which can be interpreted as cracked and incised Gilbert-type fan delta or slope deposits covered by reddish palaeosols.

After an introduction into Ancient Aigeira and its geological context (Section 2), we provide a short review of results from previous investigations at the site, which motivated this study (Section 3). We then describe the applied methods (Section 4) before presenting their results in Section 5. Finally, we discuss the consistency between the results of the different applied methods, the resolution capabilities of the FWI in combination with other methods. For a final geological interpretation, the geophysical results are compared with borehole corings.

2 | ANCIENT AIGEIRA IN ITS GEOLOGICAL SETTING

The Northern Peloponnese is home of a series of ancient poleis. Many of which are located at the southern shore of the Corinthian Gulf. In the area of the modern villages of Aigeira and Derveni at the eastern border of Archaia (Figure 1a,c), we find only a narrow coastal plain before the topography rises quickly in a step-like fashion.

Here, we find the former Ancient Aigeira on an approximately 420-m-high ridge and the neighbouring lower terraces towards the north (Papageorgiou et al., 1993; Figures 1b,c and 2a). East and
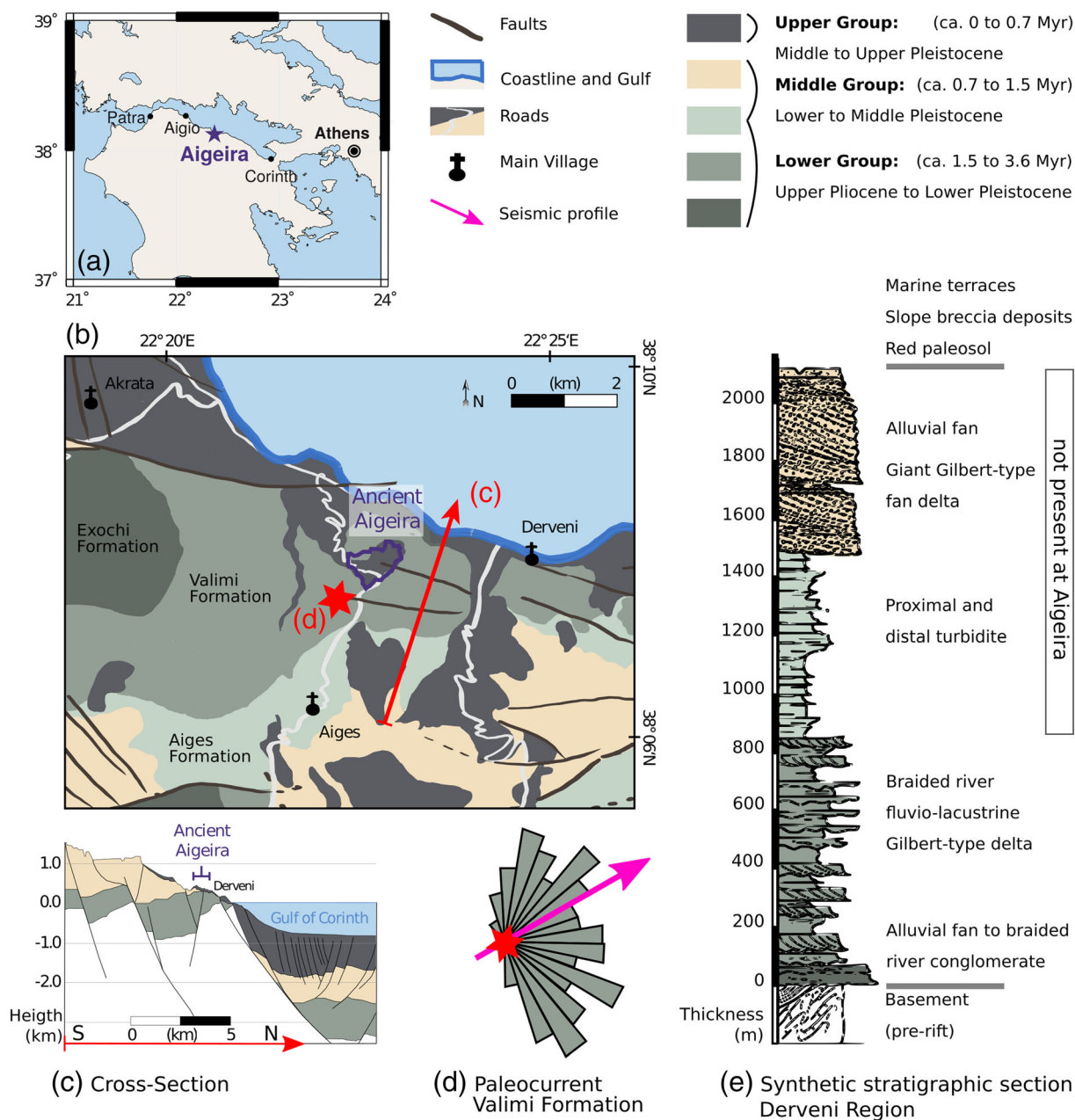
FIGURE 1 (a) Location of Ancient Aigeira. (b) Geological map of the region (after Rohais et al., 2007). (c) Cross-section along profile A (after Ford et al., 2016). (d) Direction of palaeocurrent in the Valimi formation in the Lower Group (Rohais et al., 2007) located south-west of Ancient Aigeira compared with the orientation of the seismic profile. (e) Synthetic stratigraphic section for the Derveni-Evrostini area after Rohais et al. (2007) [Colour figure can be viewed at wileyonlinelibrary.com]

west of the Aigeira plateau the landscape is deeply incised reducing Aigeira's accessibility from the south to a narrow ridge. To the north Aigeira is left overlooking the Gulf of Corinth and the coastal plain.

This ideal strategic location is most likely one reason for the long settlement history from the late Bronze Age until its fading in the late antiquity, hence making it one of the longest inhabited sites in the area (Morgan & Hall, 2004).

Excavations in Aigeira have been carried out by the Austrian Archaeological Institute in Athens (ÖAI) since 1972 and revealed that the settlement has been inhabited with occupational gaps since Middle Neolithic times (6th millennium BCE) until the 12th to early 14th century CE.

The prehistoric settlement (Neolithic, LBA, Mycenaean to Geometric times) is located on the highest grounds of the hillside (Figure 2a; 'Acropolis' and 'Saddle'). During Archaic Classical and especially in Hellenistic times, the area of the settlement was extended to the lower terraces mainly to the north. At that time, settlement extended over an area of 0.5 km² and a new public centre with a theatre (Gauß, n.d.; Gauß et al., 2016; Rusch et al., 2016), and
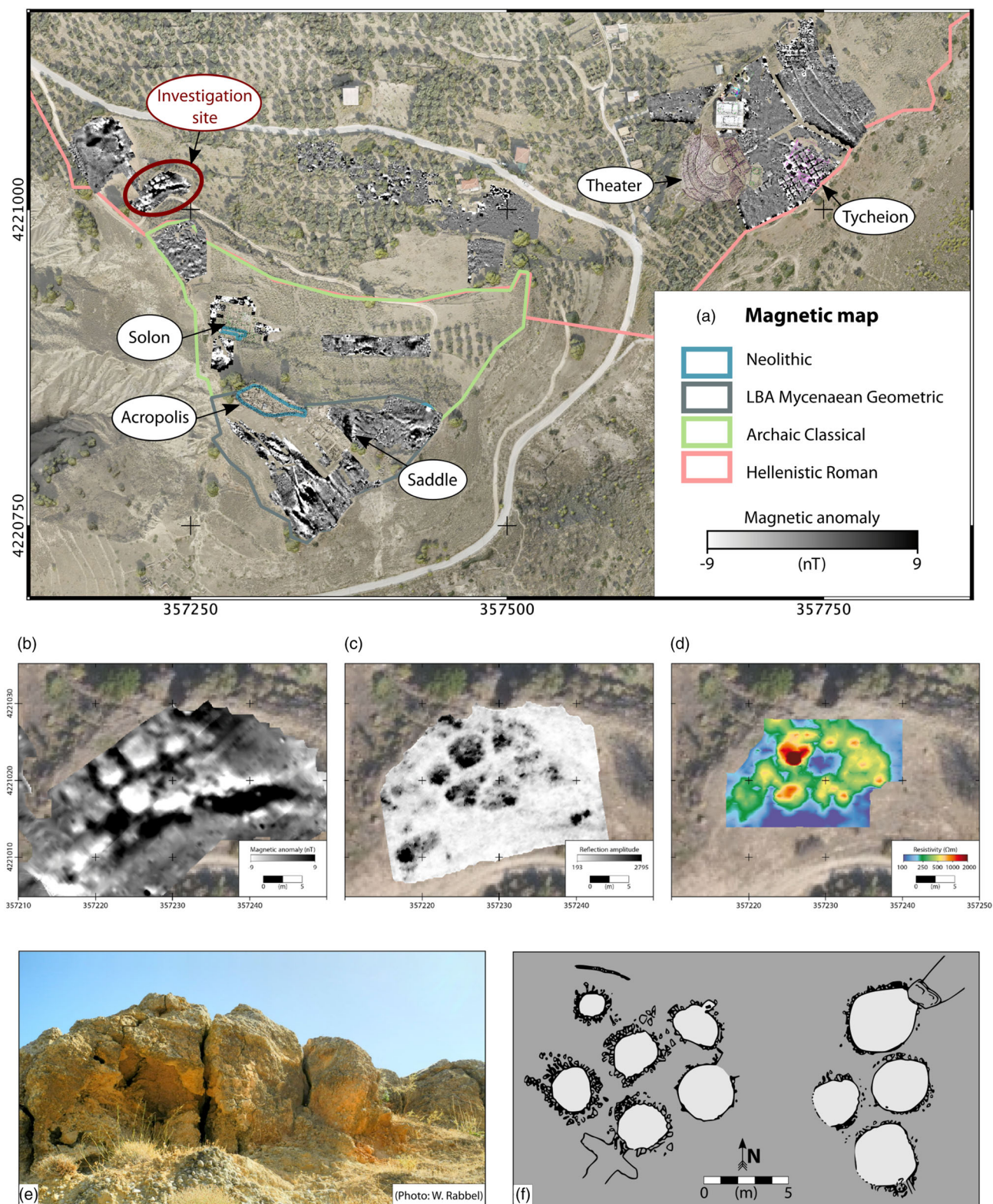
FIGURE 2 (a) Ancient Aigeira with its growing settlement dimensions overlain by the magnetic map and marked site locations. Results of first investigations at the marked investigations site; (b) magnetic map, (c) ground-penetrating radar depth slice (0.6–1.1 m) and (d) an electrical tomographic map in a depth of 0.4–0.8 m. (e) Blocks of cracked conglomerates like this one found a terrace above the survey area or (f) a system of chamber tomb like this as found by Cavanagh and Mee (1998) at another site on the Peloponnese are shown as potential interpretation options. Drone orthophoto (a–d) by Chr. Kurtze of ÖAW/ÖAI [Colour figure can be viewed at wileyonlinelibrary.com]

several temple buildings (Tanner, 2019) were constructed on a north-eastern terrace.

The step-like rise of the topography and the ridges along the southern shore of the Corinthian Gulf were formed by the processes associated with the Corinthian rift. Syn-rift sediments have been uplifted to an elevation of over 1000 m during the Quaternary in a band of 25–30 km (Ford et al., 2016; Rohais et al., 2008). These sediments with a thickness of up to 2.8 km (Ford et al., 2016; Moretti et al., 2003) cover a series of huge steps created by normal faulting. Marine terraces add to additional steps to the topography. They have been formed due to the regional uplift of the entire Peloponnese and simultaneous eustatic sea level changes.

The syn-rift sediments in Aigeira consist of the Valimi formation as part of the Lower Group of rift sediments (Figure 1b; Rohais et al., 2007) which consists of mainly Upper to Lower Pleistocene fluvio-lacustrine deposits of thin bands of granule to pebble conglomerates interbedded with mudstone and siltstone. The source of these sediments lays west–south-west of Aigeira (Figure 1d). In the layering of this formation, we can also find Gilbert-type fan deltas which again deposited coarser materials like conglomerates (Figure 1e).

The Middle Group (Lower to Middle Pleistocene) is not present in Aigeira, so sediments of the Upper Group overlay the Lower Group. This Upper Group consists of coarser materials like conglomerates in the form of slope deposits especially reddish breccias and finer grained reddish palaeosols. The latter are reworked Middle Group materials deposited in a more recent stage of the rift evolution (Rohais et al., 2007).

Tectonic deformation processes that started in the past and are still ongoing today have formed a very heterogeneous geological background that consists of features like fan deltas or weathering structures that show similar dimension of prehistoric cultural structures that are not always identifiable by their specific geometry.

In regard to the existing materials this means, that we find conglomerate, marl, mudstone and siltstone in Aigeira. The building material in Aigeira consists mainly of the locally quarried conglomerate ranging from roughly hewn conglomerate blocks used for foundations to more finely worked blocks otherwise.

Measurements of the physical properties at different investigation sites show that the magnetic susceptibilities of the present materials can be found at the almost non-magnetic end of the range (Rusch et al., 2020) and do overlap as the values for conglomerates ($\kappa = 0$–8×10^{-6} SI) and the fine-grained marl ($\kappa = 4$–9×10^{-6} SI) show. The differences in the specific electrical resistivity and the shear-wave velocity are higher. Here, the values range between $\rho = 10$–$180\,\Omega m$ for unconsolidated sediments like marl and $\rho = 140$–$7500\,\Omega m$ for the stiffer material like conglomerate. Seismic shear-wave velocities of $vs = 150$–$250\,\mathrm{m\,s^{-1}}$ for the unconsolidated sediment and $vs = 400$–$2000\,\mathrm{m\,s^{-1}}$ for the stiffer conglomerate are found. So far, no values have been measured for the reddish palaeosol, because it has not been present at geophysical investigation sites.

3 | INVESTIGATION SITE AND MOTIVATION

The aim of geophysical investigations within the framework of archaeological studies is the mapping of settlement and infrastructure remains in the subsurface such as buildings and fortification walls but also the detection of possible cemeteries.

The archaeological target investigated in this study is located on a small terrace three steps down north-west of the acropolis and right outside of the Archaic Classical settlement next to the modern path further uphill (Figure 2a). It presents a case study of a potential cemetery site, which is especially interesting because information about cemetery sites are sparse for Aigeira in general.

The Aigeira site has been investigated geophysically since 2012 (Gauß, n.d.; Gauß et al., 2016; Rusch et al., 2016). Major results were presented inter alia by Rusch et al. (2020) who also summarized geological challenges of archaeogeophysical prospecting typically connected with the syn-rift setting, to which Aigeira belongs. In the present study, we focus on a honeycomb-shaped anomaly pattern that was revealed by an initial magnetic mapping of the Aigeira site (Figure 2b). This resembles in form, size and location a possible system of Mycenaean chamber tombs found on the Peloponnese (Figure 2f; Cavanagh & Mee, 1998), motivating further geophysical investigations.

As outlined in Rusch et al. (2020), additional investigations with GPR (Figure 2c) and ERT (Figure 2d) have uncovered similar patterns. However, the results were not conclusive enough to decide without doubt if this feature is indeed caused by a system of buried or partially filled cavities that could indicate the presence of chamber tombs (Figure 2f; Cavanagh & Mee, 1998) or are related to geological structures consisting of conglomerate blocks embedded in the surrounding marl (Figure 2e).

Therefore, seismic measurements were added to complement the preceding measurements. Additionally, six cores were drilled to ground truth the results of the geophysical methods.

4 | METHODOLOGY

To determine the nature of the structure causing the observed honeycomb-shaped magnetic anomaly, we applied GPR, ERT and shear-wave seismics (Figure 3) and, finally, placed some drillings for ground truthing at key points identified through the geophysical measurements. The positioning of all geophysical data was accomplished with a Leica 500/1200 DPGS setup in the Greek Coordinate System (EGSA87). The measurements are described in the following: an overview is given in Table A1 providing information about the measurement configurations and data processing parameters.

In this study, we focus on the comparison of methods for one profile (see Figure 3) that crosses three of the six potential chamber tombs. On this profile, shear-wave seismics were com-
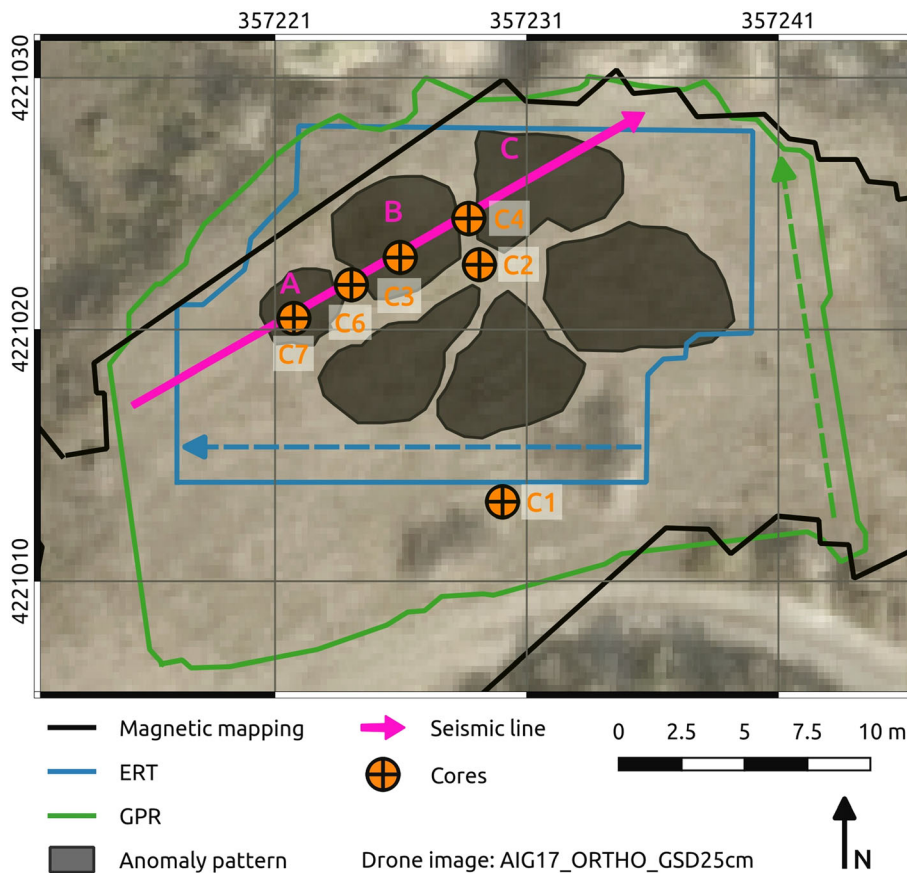
FIGURE 3 Measurements in this study mainly concentrate on the new profile along the seismic line. The profile is shown in regard to the anomaly pattern unveiled by ground-penetrating radar (GPR) with 'Cells A–C'. The extensions of the GPR and electrical resistivity tomography (ERT) areas are shown as well as their profile orientations (dashed arrows). The GPR profiles had a spacing of 0.3 m and the ERT profiles 1 m. Additionally, the locations of the cores are marked. Drone orthophoto by Chr. Kurtze of ÖAW/ÖAI [Colour figure can be viewed at wileyonlinelibrary.com]

bined with a new dual frequency GPR antenna for direct comparison. Additionally, four of the six cores were drilled along this profile for ground truthing.

4.1 | GPR and ERT

The new additional profile along the seismic line was measured with a 400-MHz and a 300-/800-MHz dual frequency antenna. For the registration, we used a SIR4000 unit. Processing was kept the same with the preceding data set (Table A1) with the only addition of the application of a gain function to compensate amplitude losses.

To include resistivity information into the comparison as well, a section along the seismic line was compiled from a set of parallel 2D ERT profiles by interpolating them along the seismic line. The interpolation was necessary because the ERT profile directions were slightly different from the seismics.

The seismic data were acquired along a linear profile with a horizontal shear-wave source radiating mainly SH waves in inline direction (Figure 4). The SH waves were excited by horizontal blows on a metal bar (Figure 4b) with a shot point spacing of 1 m and two additional shot points in the central part of the line resulting in 27 shot points along the line. The receivers, consisting of 10-Hz SH geophones, were placed with a spacing of 0.5 m along the profile (Figure 4b). The recording was conducted with a sampling interval of 0.125 s and a length of 0.5 s without applying any filters..

The first processing steps consist of a first arrival analysis using the wavefront inversion tool of the ReflexW software (Sandmeier, 2019) to estimate a long-wavelength velocity model of the subsurface. This model was interactively improved using the ray-tracing tool of the same software.

The recorded data set (Figure 5) has a high signal-to-noise ratio, but the waveforms are quite complex. It not only consists of refracted SH and Love waves but also shows local ringing and sporadic P waves converted from the prevailing SH waves at structural interfaces crossing the profile under oblique angles. We observed a significant damping of high-frequency wave portions with offset, suggesting that the soil is effectively viscoelastic with a small Q_s value. At near offsets, converted P waves interfered with the direct S wave making it often hard to pick the first S wave arrival times. Fortunately, the P waves mostly faded out within short distance, so the S wave travel times were more easy to pick at larger offsets. Here, we picked the more stable positive S phase although we see sporadic, locally occurring negative arrivals in some shot gathers which are caused by the complexity of subsoil.

4.2 | Seismics—FWI

Whereas the refraction tomography only relies on first arrival traveltimes (FATTs), the FWI is a local optimization approach that fits all waveforms (i.e., phase and amplitude) of the entire recorded field
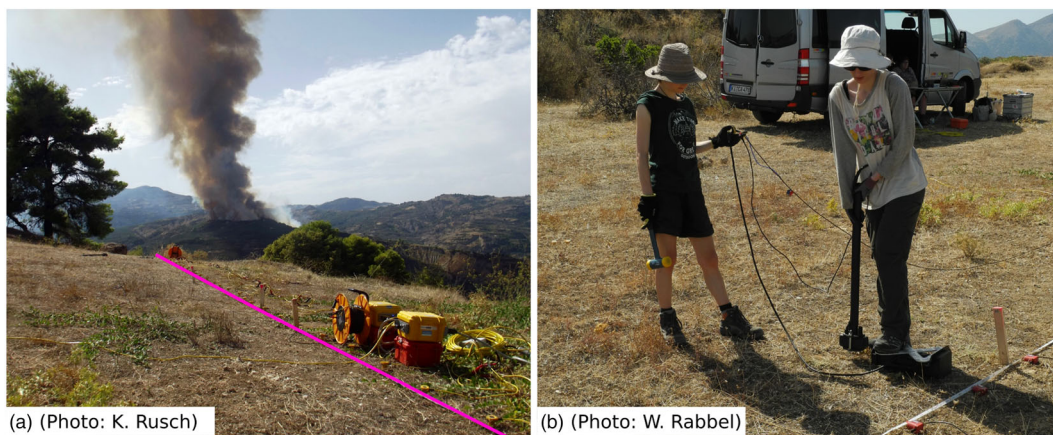
FIGURE 4 Seismic soundings. (a) View from the east on the seismic profile and (b) measurements with horizontal bar and sledgehammer as source [Colour figure can be viewed at wileyonlinelibrary.com]
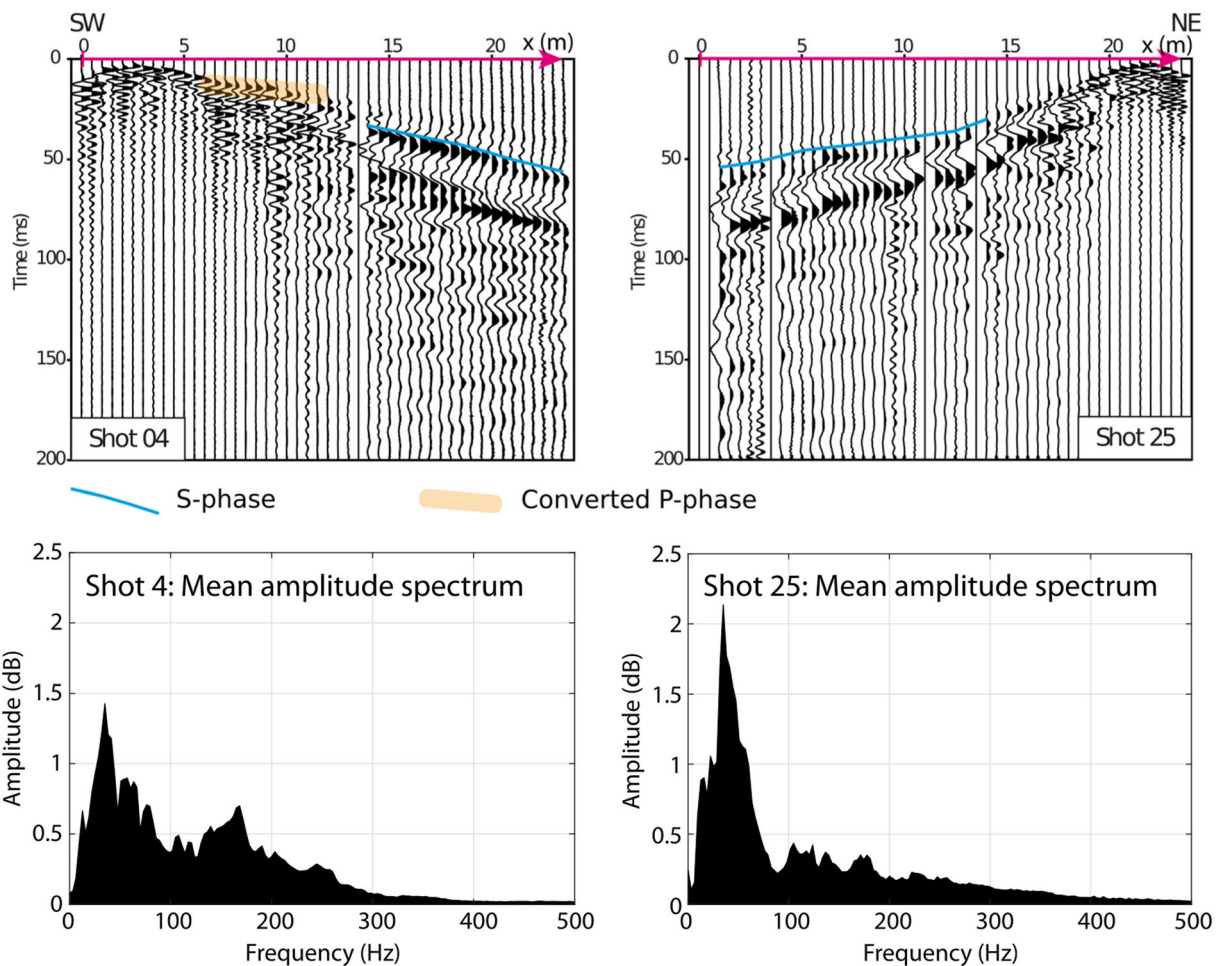

FIGURE 5 Examples of two shot gathers from the seismic survey. Important wave phases are highlighted. Seismograms are normalized to the maximum amplitude of each trace and shown without any applied frequency filter. Additionally, the mean amplitude spectra of these shots are presented in the bottom panels [Colour figure can be viewed at wileyonlinelibrary.com]

data set. Whereas the FATT resolution is restricted to the size of the first Fresnel zone, the FWI is able to resolve structures below the seismic wavelength (Devaney, 1984; Sirgue & Pratt, 2004; Wu & Toksöz, 1987).

The preprocessing steps prior to the FWI consisted of muting traces with dominant noise and an offset-dependent 3D to 2D point-to-line source and spreading correction (Forbriger et al., 2014; Schäfer et al., 2014).

As objective function for the FWI, we choose the global correlation norm (GCN; after Choi & Alkhalifah, 2012) because it was applied successfully in previous similar near-surface studies (e.g., Köhn et al., 2019; Schwardt et al., 2020). The GCN mitigates effects of an insufficient source/receiver coupling, by weighting the seismic phase higher than the amplitudes and equalizing the energy level of all traces (Dokter et al., 2017). Additionally, the difference of geometric spreading of seismic waves in a 3D medium opposed to a 2D model is compensated. The GCN also reduces the sensitivity with respect to amplitude errors (Dokter et al., 2017).

Two key aspects have to be considered for a successful FWI field data application: an accurate viscoelastic initial model of the subsurface and an inversion workflow adapted to the specific problem. The initial model describes the spatial distribution of shear-wave velocity, density and quality factor Q_s in the subsurface. An initial shear-wave velocity model was determined by a FATT analysis (Figure 6a).

The initial density model was estimated from the vs model via the empirical relation $\rho = 1000 \cdot (0.1055 \cdot \log(vs) + 1.3871)$ according to Ulugergerli and Uyanik (2007). This relation is valid for near-surface soils. A homogeneous half-space is assumed for Q_s. The best value for Q_s is chosen by running the inversion with different Q_s values and evaluating seismogram fits and the final objective function. Whereas shear-wave velocity and density are updated during the FWI, Q_s remains constant throughout the inversion. In this study, the best result was achieved using a Q_s value of 15 in regard of minimizing the objective function and regarding the fit of the amplitudes (Figures 6a and A1).

Köhn et al. (2019) compared the resolution of time-domain SH-FWI strategies based on the sequential inversion of low-pass (L) and band-pass (B) filtered data in a case study with dominating, strongly dispersive Love waves. In this study, the 'LBL' strategy resulted in the best fits. This sequential approach optimizes the model to the L filtered seismic data. With each step, the corner frequency (between 80 and 300 Hz; cf. Figure 5 and Table A2) is increased, which subsequently increases the model resolution. However, this approach is limited by the dominating low-frequency Love waves. To further improve the FWI resolution, a B filter strategy is applied to the data. Specifically, the upper corner frequency is fixed to 300 Hz, and an increasing lower corner frequency mitigates the contribution of the Love waves, while enhancing the high-frequency contributions of the reflected, refracted and diffracted seismic wavefield. This second B step can lead to a mismatch in the Love wavefield fit, which can be corrected by adding another L step with a maximum corner frequency of 300 Hz in the workflow as shown by Köhn et al. (2019).

This inversion strategy results in an accurately fit of the seismograms and amplitudes (Figures 6b,c and A2) for the high frequencies in the first 15 m of the profile and the lower frequencies for offset of 15.5–23.5 m in this rather complicated data set. Although we ignored sporadic, locally occurring arrivals in the starting model, which is based on travel time interpretation, the FWI manages to model these sporadic phases very well through incorporating corresponding structure in the model (Figures 6 and A2).

For the purpose of comparing the LBL strategy used in this study with the more commonly applied L strategy, we show a comparison of the resulting models in Figure A3.

4.3 | Ground truthing

For ground truthing, we drilled six wells. Each borehole was started with a sediment corer, and only in case of increased resistance, the drill rod was adjusted to a diamond corer and wet drilling was applied. Two of the cores were taken inside the 'cells' of the anomaly pattern, three were taken between the 'cells' and one was taken as a reference core outside the anomaly pattern. Four cores are located along the seismic profile to enable a direct comparison of the cores with the geophysical results.

The boreholes were then also used for an in situ measurement of the magnetic susceptibility. We used a Bartington MS2H down hole probe for this measurements. The probe however is only calibrated for boreholes with a diameter of 22 to 25.4 mm. Because our boreholes were drilled with a sediment corer of 0.08 m in diameter, the susceptibility values measured in situ do not represent calibrated absolute values. However, care was taken to ensure that the probe was always pressed against the borehole wall, and therefore, the trend in magnetic susceptibilities can be trusted. Repeated measurements were performed to check the reproducibility of the values and enable the computation of error bars. The measurements were taken with a vertical spacing of 0.1 m. For a drift correction, 'air' was measured before and after the measurements in the borehole, and the linear trend between these two measurements was used to correct the measurements.

5 | RESULTS

The starting point of the data interpretation is the results of previous measurements where magnetic mapping and the GPR and ERT areal measurements had revealed a honeycomb-shaped anomaly pattern (Figure 2b–d). The new data acquisition and interpretational steps were undertaken to distinguish between the following alternative interpretations of this pattern: that it might indicate either (1) a system of chamber tombs resembling literature examples or (2) a weathering structure of the local conglomerate rocks showing marl-filled fractures of honeycomb-shaped cross-section such as found in the proximity of the investigation site (Figure 2e,f; see also Rusch et al., 2020).

FIGURE 6 Full-waveform inversion (FWI). (a) Initial shear-wave velocity model, estimated by smoothing the result of the first arrival analysis. (b) Seismogram comparison of measured field data with the synthetic seismograms from the FWI result using a constant $Q_s = 15$ model. (c) Amplitude fit showing the root mean square amplitude plotted over offset [Colour figure can be viewed at wileyonlinelibrary.com]
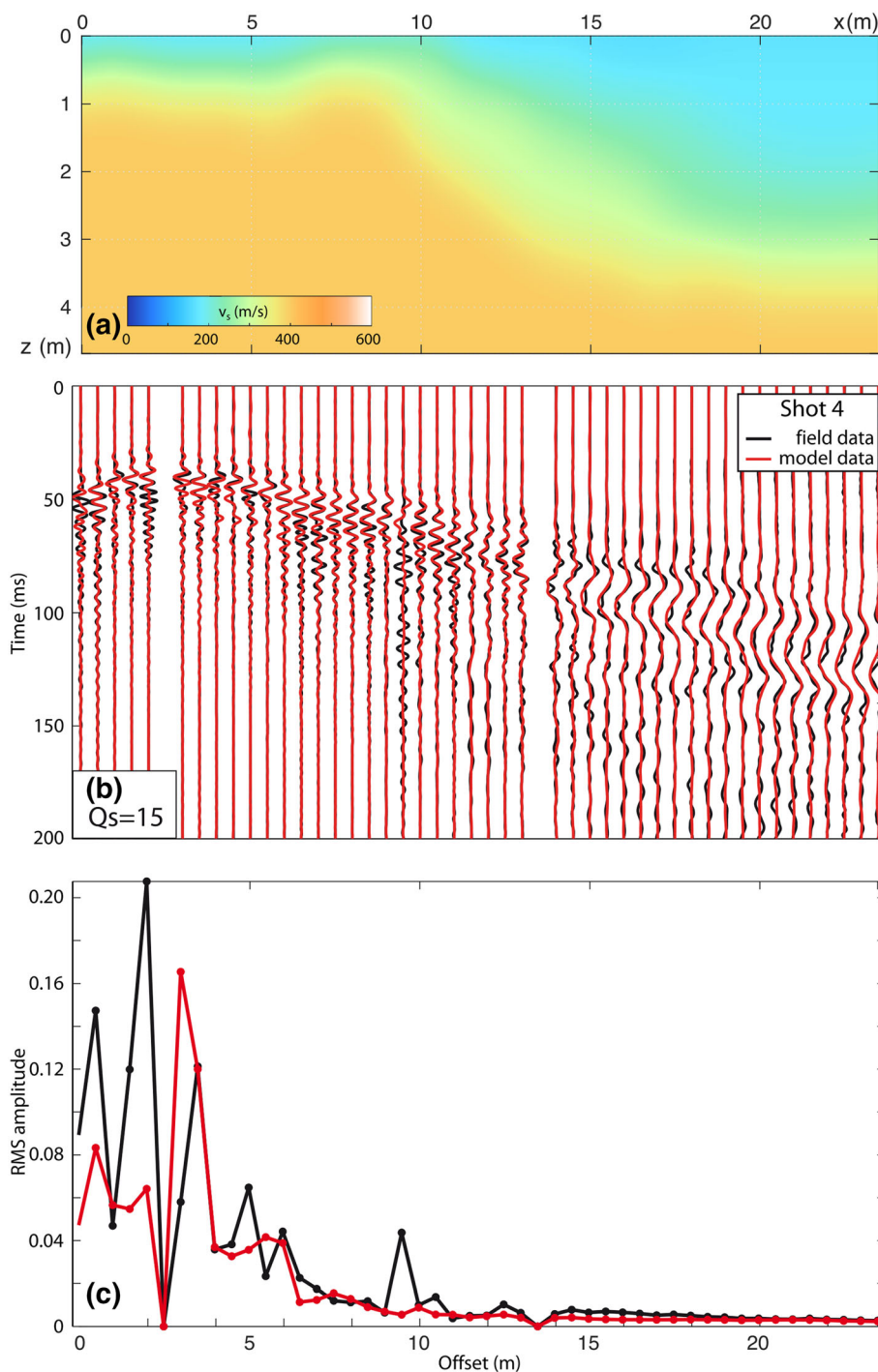
5.1 | GPR and ERT

In general, the vertical depth sections of all three antenna frequencies (300, 400, and 800 MHz; Figure 7c–e) show three zones of high reflectivity that correlate with the known Cells A–C (cf. Figure 3) confirming the preceding results.

With a penetration depth of less than 1 m, the vertical section of the 800-MHz antenna (Figure 8c) shows the upper part of the cells only but in higher resolution than the 400-MHz antenna with a penetration depth of 2 m. The 300-MHz antenna (Figure 7e) obviously

lacks in resolution compared with the 800-MHz antenna, but the comparison with the 400-MHz antenna (Figure 7d) shows no significant improvement of the image in greater depths. Therefore, we focus mainly on the results of 400-MHz antenna with some input of the 800-MHz antenna in shallow subsurface.

The 400-MHz antenna resolves in general the same structures as the 800-MHz antenna, but in the first metre, the higher resolution of the 800-MHz antenna is helpful in imaging this complex subsurface structure. In case of the dipping reflections in Cells B and C for example, the 800-MHz antenna clarifies that the seemingly coherent
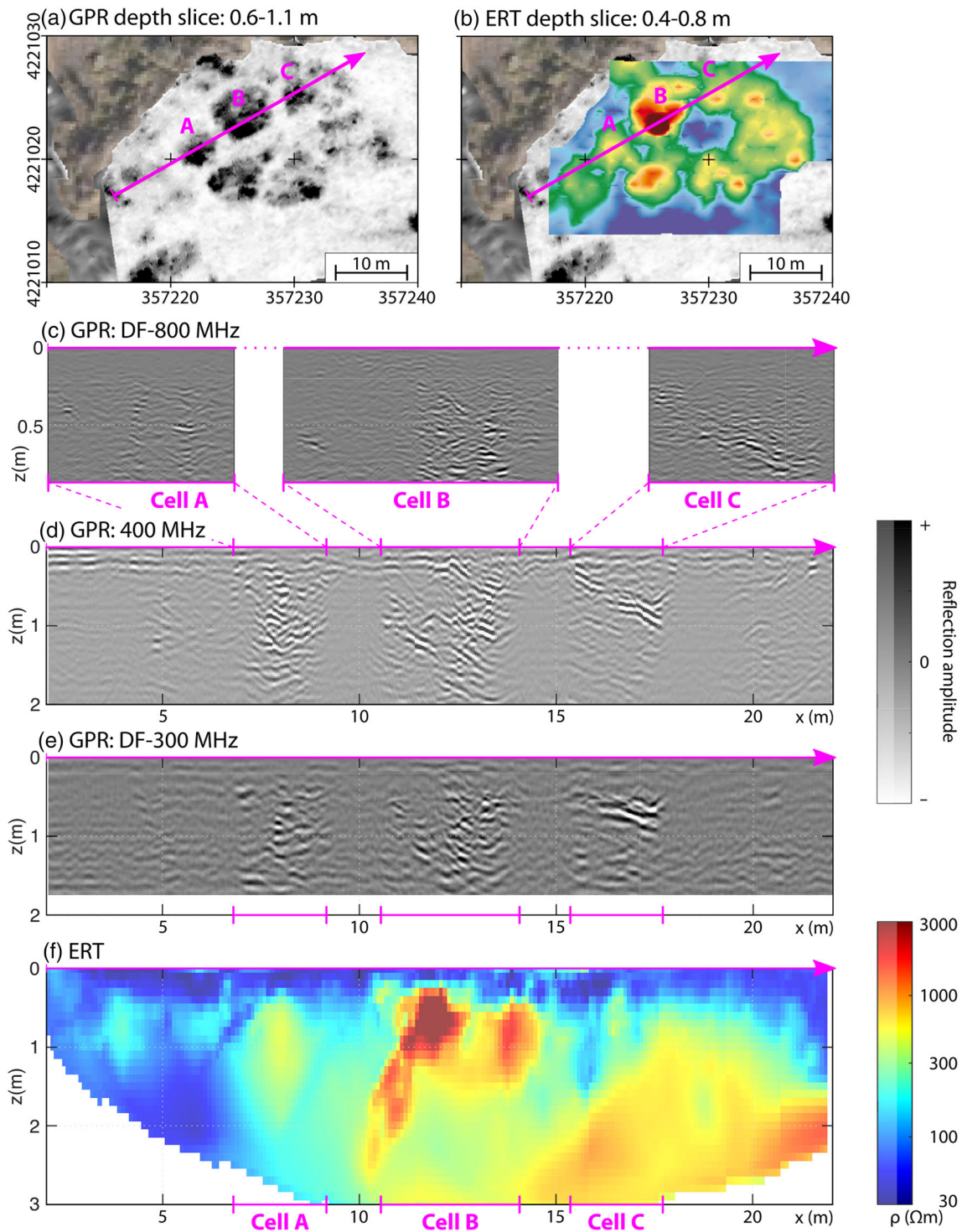
FIGURE 7 Depth slices of (a) ground-penetrating radar (GPR; 0.6–1 m) and (b) electrical resistivity tomography (ERT; 0.4–0.8 m) with the location of the new profile. GPR depth section of different antenna frequencies: zoom of the cells with (c) 800-MHz antenna, (d) 400-MHz antenna and (e) 300-MHz antenna. (f) ERT depth section. Drone orthophoto in (a) and (b) by Chr. Kurtze of ÖAW/ÖAI [Colour figure can be viewed at wileyonlinelibrary.com]

reflections are actually caused by a more complex series of small-scaled scattering bodies.

For Cell A, the top of the structure can be found in about 0.4 m. Whereas the reflections image as a thin band in the SW of the cell, they appear to reach further down in the NW half of the

cell. The internal structure of the cell is complex, but just below 1 m of depth, a north-east dipping reflection can be assumed (Figure 7c,d).

Cell B shows the most internal structure with an attenuated area in the shallow SW half and dipping reflections in the NE half and in a
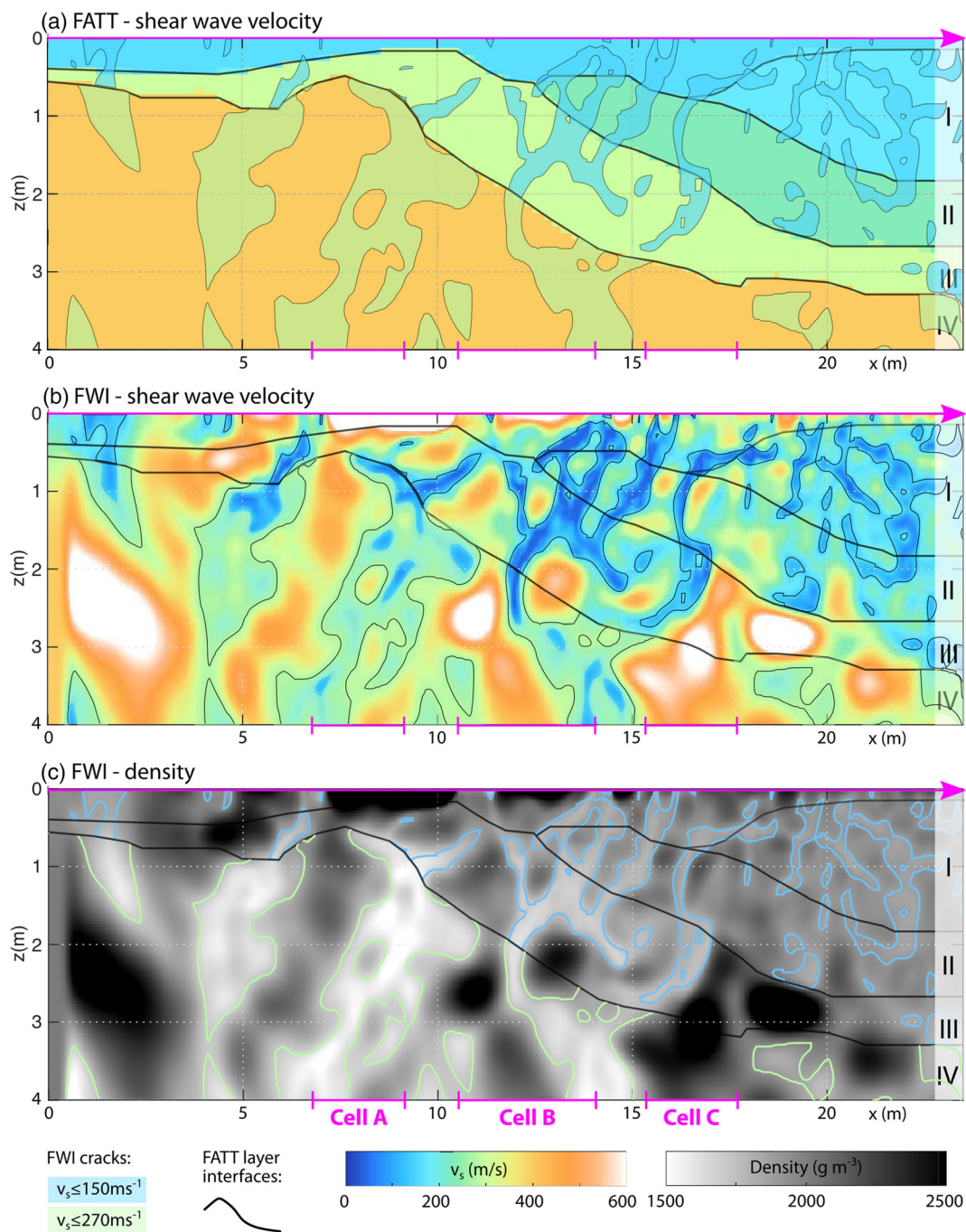
FIGURE 8 Comparison of results from first arrival traveltime (FATT) analysis and full-waveform inversion (FWI). (a) Result of FATT combined with 'crack pattern' isolated from the FWI result as areas with shear-wave velocities below 150 m s^{-1} or for layer IV a velocity below 270 m s^{-1}. (b) FWI result with marked layer interfaces from the FATT result. (c) FWI result of the density distribution with marked cracks [Colour figure can be viewed at wileyonlinelibrary.com]

depth below 0.6 m (Figure 7c,d). Cell B also shows a rather 'quiet non-reflective zone' in the centre.

The NE dipping reflections seem to continue in Cell C; however, due to the attenuated zone in between, it cannot be said for certain if or how they are connected.

Although the ERT section is extracted from the preceding ERT data set and is therefore sparsely sampled along the profile direction, similarities between the GPR and ERT (Figure 7c–f) results can be

clearly identified. The lateral changes in reflectivity in the GPR profile coincide with zones of higher resistivity values of 300–3000 Ωm whereas the zones with high attenuation map with resistivity values of around 30–200 Ωm. For Cell B, the ERT section shows extraordinary high resistivity values that coincide with the 'quiet zone' in the GPR section.

Additionally, a general dipping orientation can be assumed at the NE end of the profile.

5.2 | Seismics—FATT and FWI

The first arrival analysis of the shear-wave seismic line results in a depth section in regard to shear-wave propagation velocity.

The shear-wave velocity-depth distribution (Figure 8a) shows layers II–IV ($vs = 230$ m s^{-1}, $vs = 270$ m s^{-1} and $vs = 400$ m s^{-1}) with a dip of about 20° to 30° to the north-east below a thin layer with $vs = 160$ m s^{-1}. Additionally, the near surface in the north-east (layer I) shows slightly higher velocities than the near surface ($vs = 180$ m s^{-1}).

The seismic investigations reveal a different anomaly pattern than the preceding GPR and ERT measurements. It does not show the three cells.

The resulting subsurface model of the FWI (Figure 8b) looks rather confusing on the first glance, but it does follow the FATT model (Figure 8a) in general.

In the upper north-eastern half of the section, a wedge of lower velocities of 100 to 180 m s^{-1} is found. This matches layer I identified in the FATT results. The lower south-western half shows higher velocities in the range of 300 to 500 m s^{-1}, which can be correlated with layers II–IV.

However, compared with the results of the FATT, the FWI result is a much more detailed image of the subsurface. Whereas the general character of the results is similar, the FWI shows that the layers identified in the first arrival analysis are much more complex. Here, the layers are divided into smaller units (cm to m scale) of high velocities which are divided by a net of linear features of low velocities.

In layer I, these very slow linear features show a dip to the NE as we have seen before in the GPR and refraction seismic results. In all other layers (II–IV), these linear features are orientated more or less orthogonal to the layer interfaces of the FATT model and dip to the south-west. Some of these do also coincide with layer interfaces. It is also worth mentioning that the cracks in the layers I–III can be characterized as thin and slow ($vs < =150$ m s^{-1}); the situation in layer IV is slightly different. Here, the cracks appear broader and also less slow ($vs < =270$ m s^{-1}).

These linear features of lower velocities most likely indicate cracks in the consolidated materials that are filled or partly filled by unconsolidated sediment. This assumption is supported by the fact that these lineaments can also be found in the density distribution where they correlate with zones of lower densities (Figure 8c).

For the later comparison of the FWI results with the FATT, GPR and ERT results (Section 5.4.2), as well as the corings (Section 5.4.3), we extracted areas or rather linear elements with shear-wave velocities below 150 m s^{-1} for the shallower layers and areas of shear-wave velocities of 270 m s^{-1} for layer IV and will refer to them as 'cracks' in the following sections.

5.3 | Coring and borehole measurements

The reference core located offside of the anomaly pattern (C1; Figure 9) shows a rather fine brownish soil over the upper 2 m. Only

in the upper 0.4 m and between 1.2 and 1.4 m coarser pebbles were found. Below 1.6 m, the sediment shows a lighter brown. This brownish soil can be found in all cores that are located outside an 'anomaly cell'. So cores C4 and C2 show also the brownish soil that however becomes light brown below approximately 1- to 1.1-m depth. Core C6 that is also located between the cells, however, shows in the lower half of the core not a lighter brown unconsolidated sediment but massive conglomerate.

The cores drilled inside the cells show in the upper first 0.2 to 0.3 m a greyish fine sediment. Below that, an even finer and in case of core C3 (Cell B) nearly white sediment is found until a depth of about 0.8 to 0.9 m. Then, the transition to the conglomerate shows a transition zone with larger unconsolidated pebbles of about 0.1-m thickness. Below that, cores C6 and C7 (Cell A) show a massive conglomerate with cracks in several places.

The conglomerate in core C3 is however even more complicated in its structure. A consolidated block about 0.1-m-thick block is followed by about 0.5 to 0.6 m of unconsolidated pebbles and finer sediment before another 0.2-m-thick block of consolidated conglomerate is found, followed again by an assortment of pebbles as a transition into consolidated light brown sediment. Interestingly, core C2, which is located south of core C4 and west of core C3, shows the sediment sequence that is found in the first 0.8 m of core C3 but covered by 0.8 m of the brown soil found in cores C1 and C4.

The in situ borehole measurements (Figure 9) of the magnetic susceptibility reveal that in general, the brown soil found in the cores between the 'cells' shows significantly larger magnetic susceptibilities than does the greyish to whitish marl found inside the 'cells'. The latter appears to be as non-magnetic as does the conglomerate in the lower metre. The exception might be the greyish marl in C3. Here, the susceptibilities in the first 0.4 m are comparable with the susceptibility values of the brown soil. However, the scattering of measurements is also larger, and in the case of C2 that shows the same sequence of sediments but in greater depth, these sediments show very small magnetic susceptibilities values.

5.4 | Comparison of results of different methods

5.4.1 | Comparing FATT with GPR and ERT

In this section, we compare the results of seismic FATT and FWI results with GPR and ERT and evaluate them using the corings.

GPR and ERT results do generally compliment each other not only in the areal slices but also in the vertical sections. In the first 2 m of the subsurface, both methods show a lateral change in their respective properties (Figure 10). GPR reflections are mainly found in zones of relatively high electric resistivity whereas zones of high GPR attenuation correspond to zones of low resistivity. Inside these cells of dominant GPR reflections, even the larger internal structure seems to be mirrored in the ERT section. Both methods show indications of a dipping orientation to the north-east although the GPR reflections in
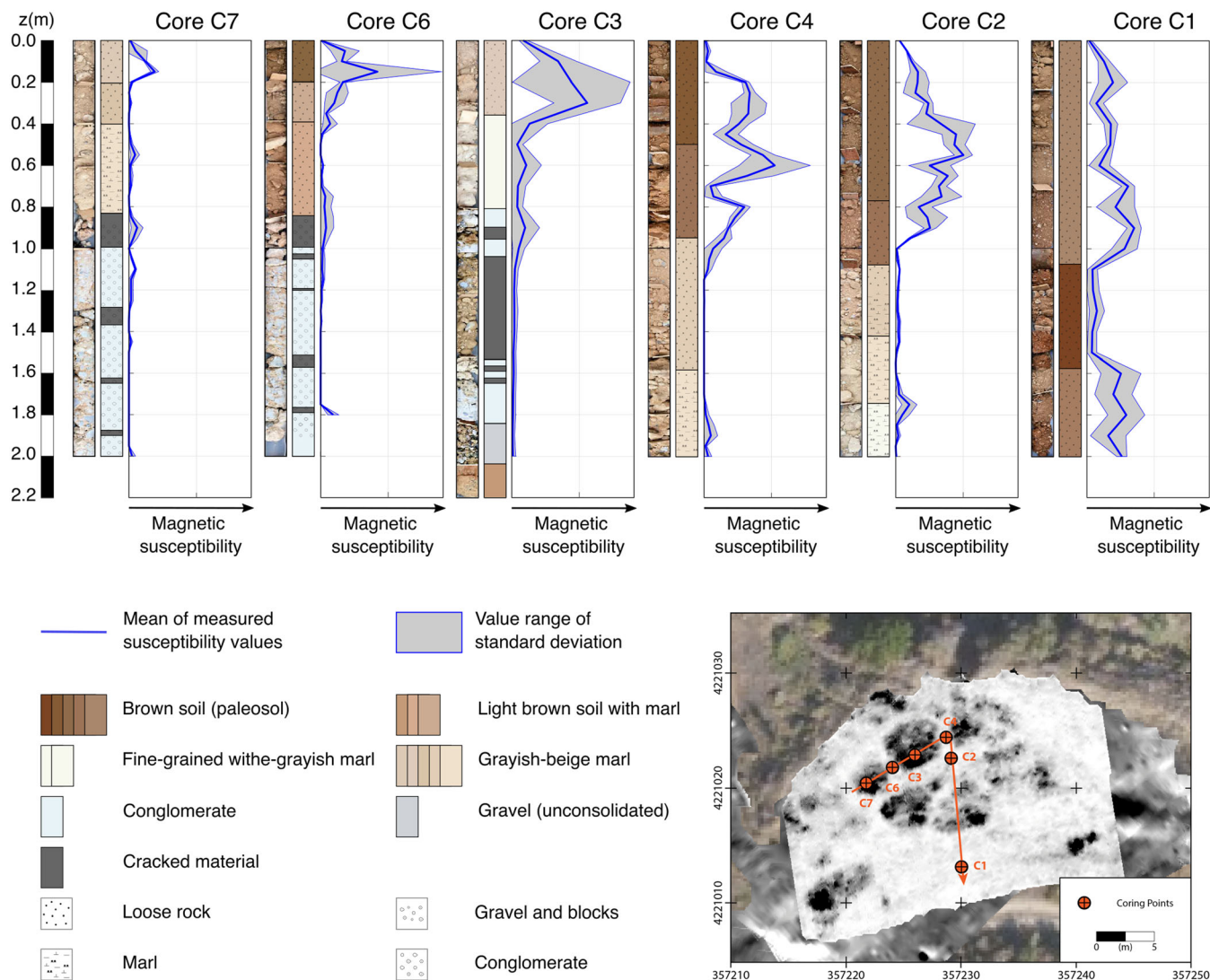
FIGURE 9 Coring results. Images of the cores, simplified stratigraphy and borehole magnetic susceptibility measurements. Cores along the seismic line (C7, C6, C3 and C4). Reference core C1. Bottom panel shows the location of the cores in relation to the GPR timeslice and seismic profile. The magnetic susceptibility can only be seen as a qualitative and relative trend, because the probe is only calibrated for smaller boreholes [Colour figure can be viewed at wileyonlinelibrary.com]

the NE do indicate a change in dip orientation to the SW. However, we can see a small mismatch in Cell B where the resistivity values show an offset to the NE and an even more distinct mismatch northeast of C4. Here, the GPR shows clear reflections directly adjacent to C4 whereas in the ERT depth section, this dipping feature begins with an offset of about 2 m. This is a 3D effect resulting from that the ERT section was not recorded exactly along GPR line but crosses it under a narrow angle and was projected on it for comparison.

The seismic velocity layers show increasing velocity values with increasing depth and also an increase in dip angle from about 20° for layer II to about 30° for the bottom layer IV (cf. Figure 10).

This result fits rather well to both the GPR and ERT results generally speaking. The orientation of the dipping reflections is mirrored in the FATT layer interfaces. Their position does also fit rather well if we keep the different resolutions of the methods in mind. For example, we do see a shift to the SW in their position

for Cells B and C, but the general fit is convincing. This includes also the upper north-eastern wedge or layer I in the FATT which coincides with the zone in the GPR section where the reflections do change dip orientation. In the case of Cell B, it is also possible that the layer interface between layers III and IV might represent the bottom of the cell, if we keep in mind that the FATT result is not a perfect subsurface model.

The comparison of the FATT result with the ERT section does affirm the impression that the ERT section shows not only lateral changes in resistivity values but that these overlay a larger structure dipping to the north-east. Here, we do see a similar mismatch as seen between ERT and GPR in the north-eastern half of the profile. This leads to a vertical offset of about 0.5 m of the layer interface between layers I and II with the ERT resistivity feature north-east of Cell C.

Besides that, the uppermost layer maps with low resistivity values as does layer I.
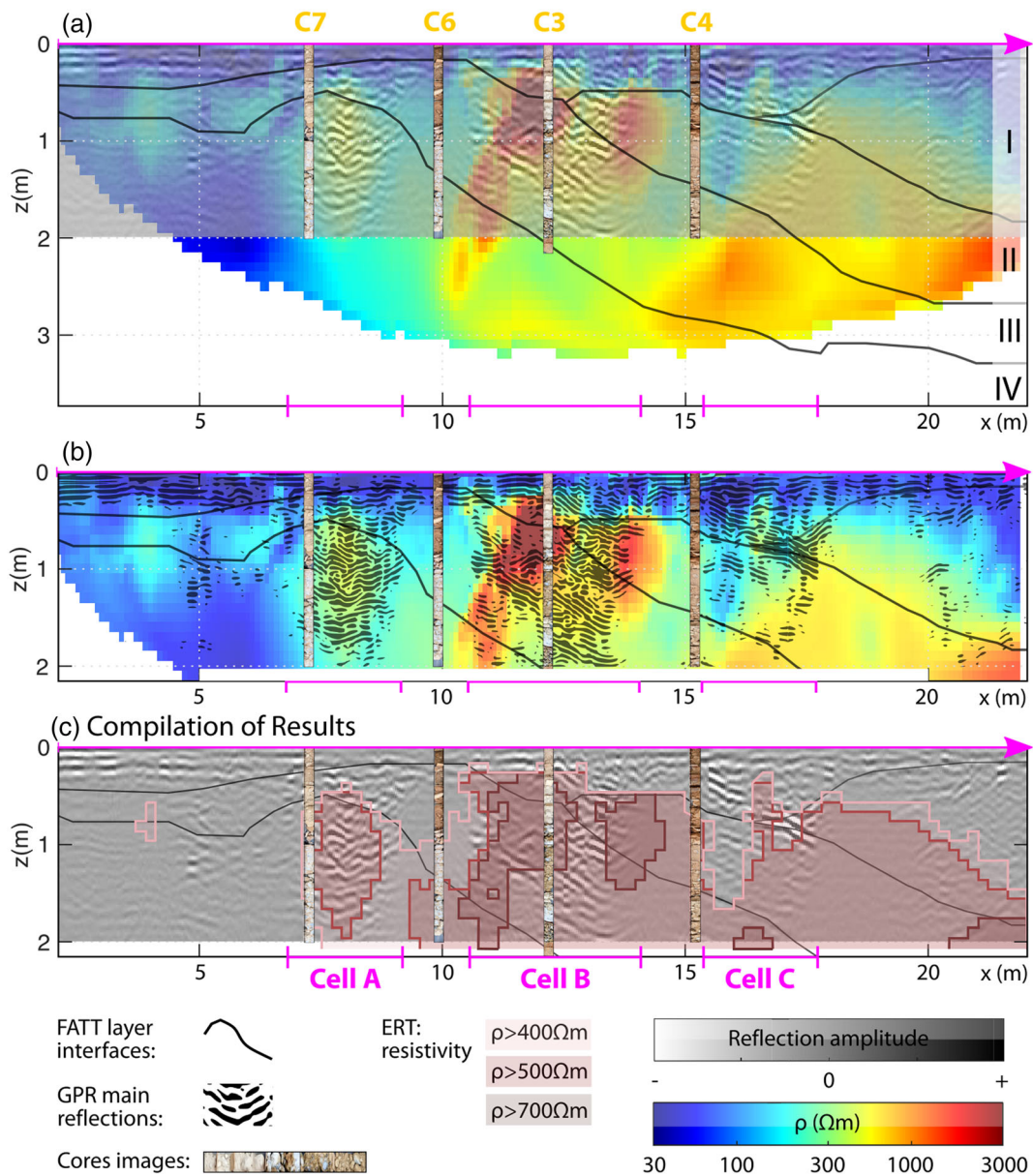
FIGURE 10 Comparison of ground-penetrating radar (GPR) and electric resistivity tomography (ERT). Shown are also the layer interfaces of the first arrival traveltime (FATT) analysis and the cores taken along the profile. (a) ERT depth section is overlain with the radargram and the cores. (b) ERT depth section overlain with only the extracted main reflections from the radargrams. (c) Radargram overlain with the isolines/areas extracted from the ERT result [Colour figure can be viewed at wileyonlinelibrary.com]

5.4.2 | Comparing FWI with GPR and ERT

The FATT result shows only a 'smoothed version' of the true shear-wave velocity distribution, which is imaged in higher detail by the FWI. The FWI result shows a much higher degree of heterogeneity and that the layers identified through FATT are in fact a complex arrangement of small-scaled units (scale: $n \cdot 10$ cm to $n \cdot 1$ m) divided by low-velocity low-density cracks. The shear-wave velocities of these smaller units are mostly higher than the average velocities obtained for the generalized layer by the FATT.

Whereas the FATT result shows only a similarly low resolution as the ERT section, the FWI results have a spatial resolution high enough to enable a detailed comparison to the GPR sections (Figure 11). An example for the high resolution is the correlation between small diffractions in the GPR section and narrow zones of higher shear-wave velocities at the north-eastern end of the profile which are divided by zones of lower seismic velocities or higher GPR attenuation, respectively (magenta box in Figure 11a).

The comparison between the results of the FWI and GPR shows that GPR reflections coincide mostly with zones of increased shear-wave velocities or at their borders. An exception is only the north-eastern edge of Cell B, where the GPR reflection seems to extend into an area with low shear-wave velocities.
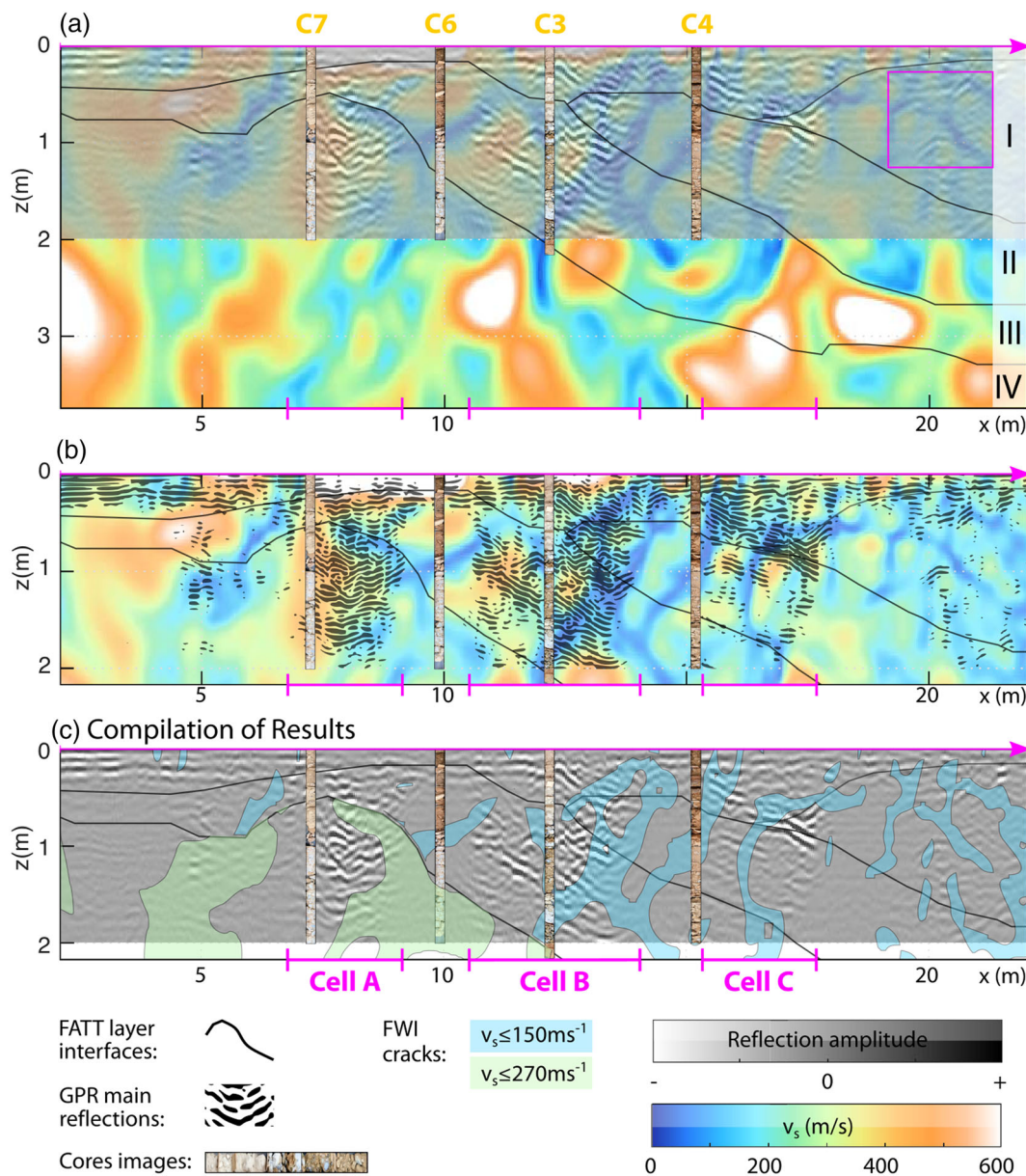
FIGURE 11 (a) Comparison of ground-penetrating radar (GPR; 400 MHz) and full-waveform inversion (FWI) results. Also shown are the layer interfaces of the first arrival traveltime (FATT) analysis and the images of the cores at their location along the profile. The magenta box marks small-scale features addressed in Section 5.4.3. (b) FWI shear-wave model overlain with only the extracted main GPR reflections. (c) GPR depth section (400 MHz) overlain with the 'cracks' extracted from the FWI result [Colour figure can be viewed at wileyonlinelibrary.com]

In the velocity-depth section, we identified fracture dominated areas by associating them with velocities $vs \leq 150$ m s^{-1} in the upper layers and $vs \leq 270$ m s^{-1} in layer IV. The resulting low-velocity zones correlate with zones of decreased density and coincide also partly with layer interfaces of the FATT and reflections of the GPR (top of Cell A or C; Figure 11c). However, most often, they run approximately perpendicular to the dip of the layer interfaces seen in the GPR and FATT sections. The dip orientation of the fractured zones is to the south-west in most parts of the section. The exception is layer I where the cracks dip to the north-

east as well. The observed change in orientation of the cracks in layer I goes hand in hand with the change in the dip of reflections from dipping to NE to dipping SW in the GPR section, so that the cracks again run perpendicular to the layering.

The comparison with the GPR result shows that the cracks can often be associated with low reflection amplitudes or seem to run along the edges of zones with high reflection amplitudes. In Cell C, a crack seems to cross an area of high reflection, but its location coincides with interruptions or steps in the reflection horizons.

5.4.3 | Integration of ground truthing and verification of geophysical results

The compilation of results so far enables us to favour a geological interpretation of the honeycomb-shaped anomaly pattern instead of potential chamber tombs. In the last step, the coring results are compared with the geophysical results. Additionally, the corings can be used as verification for the geophysical measurements, especially the FWI.

The reference core C1 offsite the anomaly pattern shows a brown soil up to a depth of 2 m, which can be viewed as the background model for the investigation site (Figure 9).

The comparison of the cores inside and outside of the cells of the pattern shows the main difference to be found in the first 0.8 to 1 m of the cores. The cores from inside the cells show a white to grey fine-grained sediment (C3 and C7; Figure 12a,b), whereas the cores outside of the cells show different shades of the brown soil (C2, C4 and C6; Figure 12a,b) also found outside the pattern in the reference core. Hence, the assumption that it is not a transition between conglomerate and marl causing the anomaly pattern but the transition between the brown soil and the whitish-greyish sediments. This is supported by measurements of the magnetic susceptibility in the boreholes. The brown soils show in general significantly higher magnetic susceptibility values compared with the whitish-greyish sediments.

The ERT measurements show that the material between the cells is also more electrically conductive with resistivity values in the order of 30 Ωm at the near surface so that the brown soil could also be the cause of the high attenuation of the electromagnetic radar waves (Figure 10). So this near-surface change in materials could explain not only the magnetic but also the GPR and ERT anomaly pattern.

As mentioned before, we can also use the coring results to validate our geophysical results, and we do indeed see a great agreement between the geophysical and the coring results.

The GPR reflections in the 400-MHz depth section correlate with the transition from unconsolidated sediment to the consolidated conglomerate (B1 and B3; Figure 12a), and the results of the 800-MHz antenna show also the transitions between the different unconsolidated sediments (B1, B3 and B4). Core C3 not only agrees well with the transitions between looser sediment and conglomerate rock but also maps the internal structure inside the cell, so that the GPR reflections perfectly surround the heavily cracked conglomerate found in a depth of 1 to 1.5 m. Here, the conglomerate is heavily cracked and shows a high cracked porosity.

We find a nearly perfect fit of cracks in the FWI and cracked conglomerate in the cores C6 and C3 (B2 and B3; Figure 12b). Here, the identified cracks coincide with zones of highly cracked conglomerate or bigger unconsolidated pebbles. For core C4, the crack does not correlate with cracked conglomerate but with the transition between the brown soil and the more finer grained greyish-beige marl. For core C7, we do see cracked conglomerate in the core, but no crack was identified in the FWI result in this particular zone.

6 | DISCUSSION

The decision if an anomaly pattern detected by geophysical surveys is caused by a geological structure or by cultural heritage in the subsurface can be often difficult to make, especially if a prehistoric heritage is sought or expected where clear typical geometric forms like rectangular houses are missing. The case study in this article shows that seismic soundings and the application of a FWI can help making this decision, and in this section, we present a possible geological interpretation of the anomaly pattern before discussing the aspect of consistency between the applied methods and usefulness of combinations of these methods and addressing the resolution capabilities of the FWI compared with previous findings.

6.1 | Geological interpretation of the geophysical results

The results of the geophysical investigations have shown that the anomaly pattern is indeed not caused by cultural heritage but by a highly heterogeneous geological structure, so that no archaeological but a geological interpretation is sought. An attempt of an interpretation of these complex arrangement of conglomerate marl and brown soil is shown in Figure 12c.

To understand how a structure like this was created, we have to go back to the recap of the geological past since the Upper Pleistocene of this region (compare Section 2). Aigeira is located in the belt of syn-rift sediments deposited during the evolution of the Corinthian rift. After Rohais et al. (2007), we find here only the Valimi formation as part of the Lower Group which is covered by the Upper Group. The Valimi formation consists of thin bands of granule- to pebble-sized conglomerates ($h = 0.5$ to 10 m) interbedded into the mudstones and siltstones. But we do also find slope deposits and Gilbert-type fan deltas (Figure 1e).

Rohais et al. (2007) also provide data for the palaeocurrents in the Valimi formation for the region. A general orientation from west–south-west to east–north-east can be seen for the Derveni region and also for a location only few kilometres south-west of Aigeira (cf. Figure 1d). This orientation equals the orientation of our seismic profile.

These Gilbert-type fan deltas do also show a steep internal stratigraphy (Rohais et al., 2007) with dips of 10° to 30°, thicknesses of 0.1 to 1 m.

All this does sound familiar, if we recall our geophysical results on a profile that follows the orientation of deposition of these Gilbert-type fan deltas. We do see a general dip of about 20° to 30° in profile direction and therefore in the direction of the palaeocurrent.

During all this, we should not forget the regional tectonic forces of fault activity and uplift or as Rohais et al. (2007) call it 'brutal surface uplift' during the Upper Group deposition. These processes can, of course, cause the cracking of the deposited materials found in our study.
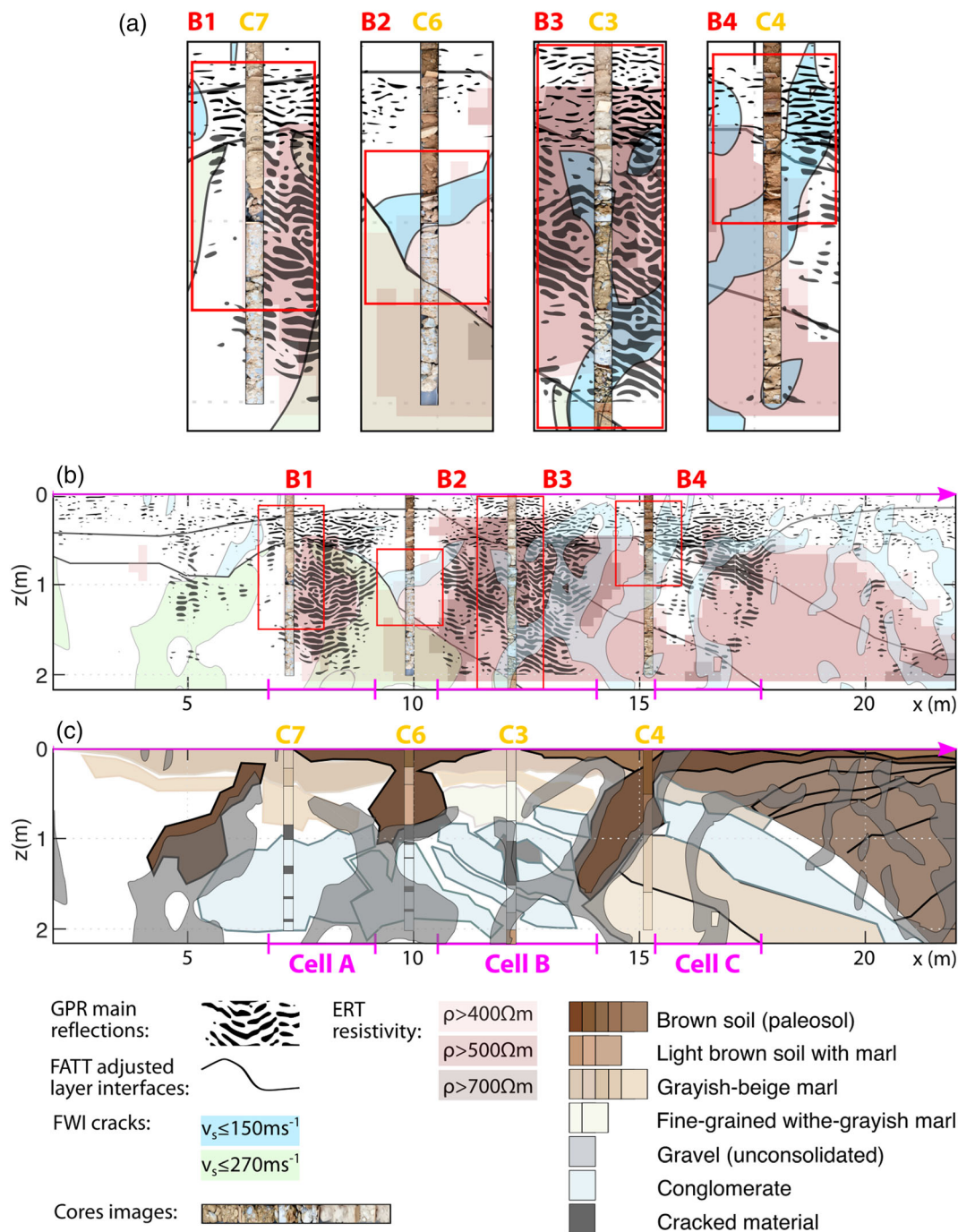
FIGURE 12 (a) Zoom on the four cores with marked boxes that show the fit between the geophysical results and the corings. (b) The extracted main features of the different results (layer interfaces of the first arrival traveltime [FATT], cracks isolated from the full-waveform inversion [FWI], main ground-penetrating radar [GPR] reflections [0–0.5 m: 800-MHz antenna and 0.5–2 m: 400-MHz antenna] and resistivity areas of the electrical resistivity tomography [ERT]) are shown. (c) An attempt of a geological interpretation that includes all inputs [Colour figure can be viewed at wileyonlinelibrary.com]

It also favours erosion, and during the Upper Group deposition, existing Gilbert-type fan deltas were indeed incised again. During this phase of rift evolution, materials of the Middle Group were reworked, and reddish breccias and finer grained deposits of fersiallitic soils (red palaeosol) were formed and deposited on top of the reincised fan deltas which could explain the presence of the brown soil we find incised in our case study.

6.2 | How consistent are the results of the different methods with the FWI model?

After the discussion of the archaeological and geological questions, we now turn to discussing methodological issues.

During this case study, the geophysical methods have shown generally compatible results. Generally, we see a correlation between

good GPR reflectivity, higher resistivity values and higher shear-wave velocities, as well as the high GPR attenuation, low resistivity values and lower shear-wave velocities. But we also identified a few exceptions we would like to discuss here.

Deviations between the layer interfaces and the GPR reflections can be traced to the different resolutions of the two methods.

We have seen a shift and thereby mismatch of ERT results especially in the north-eastern half of the profile. This concerns the comparability with the top of layer II in the FATT and Cell C. Additionally, the GPR reflectivity and the zones of high resistivity values do not match perfectly in Cell B, where we also find extraordinarily high resistivity values that coincide with low reflectivity and have no correspondence in the coring. These mismatches are certainly caused by that the ERT section represents an interpolated cross-line image compiled from parallel profiles that run sideways of the presented section, so that we see a projection on this line of the highly heterogeneous 3D subsurface to the side.

In contrast to the case in C7, the cracked conglomerate in C6 does coincide with a 270-m s^{-1} crack. Whereas core C6 is located between the cells in a zone with varying shear-wave velocities, core C7 is located in the centre of a high velocity block of Cell A which might also be a reason why the FWI did not pick up on the crack.

Generally, the FATT model is required as an initial starting point for the FWI, and it is always best to supplement the FWI with as many additional methods as possible, but was one method more insightful than the other in this study?

Other authors have already shown that the ERT may help confirming or evaluating the large-scaled structure revealed by FWI. Schwardt et al. (2020) showed a correlation between the bulk structures found by FWI and ERT in Ainos, Turkey, and in a study by Wilken et al. (2019), the ERT measurements provide the gross structure of the location and extension of the buried canal Fossa Carolina. The same can be said for our case study where the ERT measurements give us a simplified insight in the subsurface structures but are not nearly as detailed as the FWI results.

Regarding fracture patterns, it has to be added that the electrical current will use moisture- or clay-enriched crack fillings as 'preferred pathways' through the subsurface, which results in strongly modified bulk resistivity values of the larger rocks but usually does not enable mapping these cracks from the earth surface.

The combination of GPR and FWI is more important in this case study, despite the laterally alternating attenuation. In the cells, the GPR shows complex internal structures. In between the cells, the FWI with its high spatial resolution is able to provide an image of the spaces between the cells and bridge the gaps between the GPR insights so to say. The GPR also has the important additional advantage that it can distinguish between the different sedimentary units, which are not identifiable in the FWI results.

Lastly, the corings were not only useful in verifying the geophysical results but also helped immensely in understanding the complex subsurface structure. Without them, the presence of the brown soil might have only be suspected due to the low resistivity values, the high attenuation and the missing insight for the high magnetization between the cells, so that targeted coring can be vital in a complex case like this one.

6.3 | Potential of the FWI

For a successful FWI of a viscoelastic medium, a good initial model has to be determined as a starting point that fits first breaks and the amplitudes and dispersion of the Love wave sufficiently well. In our case, this could be achieved by FATT providing a rather undifferentiated shear-wave velocity model, to which a density model was attributed through a linear velocity-density relation, and the assumption of a homogeneous Q_s model. Additionally, an inversion strategy is needed that results in a good compromise between model smoothness and data fit. In this study, this is achieved by the used sequential LBL-inversion strategy (Köhn et al., 2019).

The smoothing of the gradients during the inversion by 3/4 of the local wavelength in horizontal and 1/4 in z direction dampens potential kernel artefacts so that the identified cracks in the results are real features of the subsurface and no inversion artefacts of the inversion algorithm to achieve a better data fit.

Using this approach, we achieved a FWI result with a spatial resolution on the decimetre scale that is generally supported by the results of GPR and ERT and additionally verified by corings. The fit between FWI result and coring is especially convincing for the two central cores, where the isolated cracks can be clearly correlated with the cracked materials in the cores and with disruptions in the GPR reflections.

Previous studies show that this spatial resolution is impressive but not at all outlandish. Dokter (2015) and Dokter et al. (2017) have conducted synthetic tests and found a function of resolution depending on the depth of the target. So that a structure on a 1-m scale can be imaged in a depth of up to 4 m at a mean background velocity of 220 m s^{-1} with the FWI. More recently, Schwardt et al. (2020) have shown that the FWI is capable to image an about 0.8-m-thick layer of grey sand below 1 to 1.5 m of loamy silt more reliable than other applied methods like ERT or electromagnetic induction. Their result was verified by a coring. The study of different inversion strategies by Köhn et al. (2019) shows that sediment changes on a scale of 0.2 to 0.5 m can be resolved as validated by an excavation., thereby proving advanced resolution capabilities of the FWI and its usefulness in archaeological questions that deal with small-scaled (below 1 × 1 m) sedimentary changes with the presented inversion workflow.

The studies mentioned above examined differences in sediments like sand layer in silt surrounding or layers of clay in an old riverbed. In this study, the differentiation between sediments is not possible through the FWI but by the GPR; however, the detection of cracks on a decimetre scale within the first 2 m of the subsurface has to our knowledge never been seen before. Studies that concentrate on cracks or fracture detection generally focus on larger geological scales or petroleum geophysical investigations.

7 | CONCLUSION

In this case study, we investigated an anomaly pattern found in Ancient Aigeira as an example for a prehistoric archaeogeophysical case where it is unclear if an anomaly is caused by cultural heritage or 'only' by a geological structure.

The investigations were conducted by applying a wide spectrum of methods: GPR, ERT, FATT, FWI and corings. The geophysical methods revealed generally consistent results and have been confirmed by cores. The sequential LBL-FWI strategy has revealed a highly heterogeneous subsurface model with a spatial resolution on decimetre scale. The resulting model is characterized by cracks running mostly perpendicular to the dipping FATT layer interfaces and GPR reflections. The addition of GPR gives insight in the internal structure of the identified cells and can distinguish between different sediments, where the FWI can bridge the gaps in the GPR caused by high attenuation. The cores are used not only as verification of the geophysical results but also vital in the understanding of the complex subsurface and the materials involved.

A combination of FWI (with a rough FATT result as initial model), GPR and targeted corings were identified as a valid combination of methods to interpret the anomaly pattern found in Ancient Aigeira.

In this particular case, we are confident in our interpretation that the honeycomb-shaped anomaly pattern is not caused by chamber tombs but by geological structures that might be explained by slope deposits or a reincised Gilbert-type fan delta of the Valimi foundation that was than draped by fersiallitic soils.

CONFLICT OF INTEREST

The authors declare no conflict of interest.

DATA AVAILABILITY STATEMENT

The data that support the findings of this study are available from the corresponding author upon reasonable request.

ORCID

Katharina Rusch https://orcid.org/0000-0002-6670-7864

REFERENCES

Alam, M. I. (2019). Near-surface characterization using traveltime and full-waveform inversion with vertical and horizontal component seismic data. *Interpretation*, 7, T141–T154. https://doi.org/10.1190/INT-2018-0132.1

Athanasopoulos, N., & Bohlen, T. (2017). Aquifer characterization using elastic full-waveform inversion. *23rd European Meeting of Environmental and Engineering Geophysics European Association of Geoscientists & Engineers*, 2017, 1–5. https://doi.org/10.3997/2214-4609.201702018

Cavanagh, W. G., & Mee, C. (1998). *A private place: Death in prehistoric Greece*. Jonsered.

Choi, Y., & Alkhalifah, T. (2012). Application of multi-source waveform inversion to marine streamer data using the global correlation norm. *Geophysical Prospecting*, 60, 748–758. https://doi.org/10.1111/j.1365-2478.2012.01079.x

Davis, J. L., & Annan, A. P. (1989). Ground-penetrating radar for high-resolution mapping of soil and rock stratigraphy. *Geophysical Prospecting*, 37, 531–551. https://doi.org/10.1111/j.1365-2478.1989.tb02221.x

Devaney, A. J. (1984). Geophysical diffraction tomography. *IEEE Transactions on Geoscience and Remote Sensing*, GE-22, 3–13. https://doi.org/10.1109/TGRS.1984.350573

Dokter, E. (2015) 2D time domain waveform inversion of a near surface SH wave data set from Čachtice, Slovakia. Ph.D. thesis, Kiel University.

Dokter, E., Köhn, D., Wilken, D., De Nil, D., & Rabbel, W. (2017). Full waveform inversion of SH- and Love-wave data in near-surface prospecting. *Geophysical Prospecting*, 65, 216–236. https://doi.org/10.1111/1365-2478.12549

Forbriger, T., Groos, L., & Schäfer, M. (2014). Line-source simulation for shallow-seismic data. Part 1: Theoretical background. *Geophysical Journal International*, 198, 1387–1404. https://doi.org/10.1093/gji/ggu199

Ford, M., Hemelsdaël, R., Mancini, M., & Palyvos, N. (2016). Rift migration and lateral propagation: Evolution of normal faults and sediment-routing systems of the western Corinth rift (Greece). *Geological Society Special Publication*, 439, 131–168.

Gauß, W. (ed.) (n.d.) Aigeira 3. Forschungen im Bereich des Theaters 2011–2018. Forschungen in Aigeira, Band: *3*. (Wien [in print]).

Gauß, W., Smetana, R., Rutter, J. B., Regner, C., Rusch, K., Stümpel, H., … Hinker, C. (2016). Aigeira 2013 – 2014 Bericht zu Aufarbeitung und Grabung. *Jahreshefte des Österreichischen Archäologischen Institutes in Wien*, 84, 11–50.

Günther, T., Rücker, C., & Spitzer, K. (2006). Three-dimensional modelling and inversion of dc resistivity data incorporating topography—II. Inversion. *Geophysical Journal International*, 166, 506–517. https://doi.org/10.1111/j.1365-246X.2006.03011.x

Köhn, D., Wilken, D., De Nil, D., Wunderlich, T., Rabbel, W., Werther, L., … Linzen, S. (2019). Comparison of time-domain SH waveform inversion strategies based on sequential low and bandpass filtered data for improved resolution in near-surface prospecting. *Journal of Applied Geophysics*, 160, 69–83. https://doi.org/10.1016/j.jappgeo.2018.11.001

Krampe, V., Pan, Y., & Bohlen, T. (2019). Two-dimensional elastic full-waveform inversion of love waves in shallow vertically transversely isotropic media: Synthetic reconstruction tests. *Near Surface Geophysics*, 17, 449–461. https://doi.org/10.1002/nsg.12061

Loke, M. H., & Barker, R. D. (1995). Least-squares deconvolution of apparent resistivity pseudosections. *Geophysics*, 60, 1682–1690. https://doi.org/10.1190/1.1443900

Mecking, R., Meinecke, M., Erkul, E., Driehaus, B., Bolten, A., Pirson, F., & Rabbel, W. (2020). The Yığma Tepe of Pergamon: Stratigraphic construction of a monumental tumulus from seismic refraction

measurements. *Archaeological Prospection*, 27, 73–105. https://doi.org/10.1002/arp.1762, https://doi.org/10.1002/arp.1762

Moretti, I., Sakellariou, D., Lykousis, V., & Micarelli, L. (2003). The Gulf of Corinth: An active half graben? *Journal of Geodynamics*, 36, 323–340. https://doi.org/10.1016/S0264-3707(03)00053-X

Morgan, C., & Hall, J. M. (2004). *Achaia* (pp. 472–488). OUP.

Papadopoulos, N., Tsourlos, P., Tsokas, G., & Sarris, A. (2007). Efficient ERT measuring and inversion strategies for 3D imaging of buried antiquities. *Near Surface Geophysics*, 5, 349–361. https://doi.org/10.3997/1873-0604.2007017

Papageorgiou, S., Arnold, M., Laborel, J., & Stiros, S. C. (1993). Seismic uplift of the harbour of ancient Aigeira, Central Greece. *International Journal of Nautical Archaeology*, 22, 275–281. https://doi.org/10.1111/j.1095-9270.1993.tb00420.x

Polymenakos, L., & Tweeton, D. (2017). Non-invasive characterization of a burial tumulus with use of seismic P-wave velocity and attenuation tomography. *Journal of Archaeological Science: Reports*, 13, 36–48. https://doi.org/10.1016/j.jasrep.2017.03.025

Rabbel, W., Stümpel, H., & Woelz, S. (2004). Archeological prospecting with magnetic and shear-wave surveys at the ancient city of Miletos (western Turkey). *The Leading Edge*, 23, 690–693+703.

Rohais, S., Eschard, R., Ford, M., Guillocheau, F., & Moretti, I. (2007). Stratigraphic architecture of the Plio-Pleistocene infill of the Corinth Rift: Implications for its structural evolution. *Tectonophysics*, 440, 5–28. https://doi.org/10.1016/j.tecto.2006.11.006

Rohais, S., Eschard, R., & Guillocheau, F. (2008). Depositional model and stratigraphic architecture of rift climax Gilbert-type fan deltas (Gulf of Corinth, Greece). *Sedimentary Geology*, 210, 132–145. https://doi.org/10.1016/j.sedgeo.2008.08.001

Rücker, C., Günther, T., & Spitzer, K. (2006). Three-dimensional modelling and inversion of dc resistivity data incorporating topography—I. Modelling. *Geophysical Journal International*, 166, 495–505. https://doi.org/10.1111/j.1365-246X.2006.03010.x

Rusch, K., Stümpel, H., Gauß, W., Müth, S., Kissas, K., & Rabbel, W. (2020). Geological challenges of archaeological prospecting: The Northern Peloponnese as a type location of populated syn-rift settings. *Remote Sensing*, 12, 2450. https://doi.org/10.3390/rs12152450

Rusch, K., Stümpel, H., & Rabbel, W. (2016). Geophysikalische Untersuchung im Theaterbereich von Aigeira. In G. Schörner & K. Meinecke (Eds.), *Akten des 16. Österreichischen Archäologentages am Institut für Klassische Archäologie der Universität Wien vom 25. bis 27. Februar 2016* (pp. 417–420). Phoibos Verlag.

Sandmeier, K.-J. (2019) ReflexW Version 8.5 WindowsTM XP/7/8/10-program for the processing of seismic, acoustic or electromagnetic reflection, refraction and transmission data. https://www.sandmeier-geo.de/Download/reflexw_manual_a4.pdf. Accessed: 2020-07-28.

Schäfer, M., Groos, L., Forbriger, T., & Bohlen, T. (2014). Line-source simulation for shallow-seismic data. Part 2: Full-waveform inversion—A synthetic 2-D case study. *Geophysical Journal International*, 198, 1405–1418. https://doi.org/10.1093/gji/ggu171

Schwardt, M., Köhn, D., Wunderlich, T., Wilken, D., Seeliger, M., Schmidts, T., ... Rabbel, W. (2020). Characterization of silty to fine-sandy sediments with SH waves: Full waveform inversion in comparison with other geophysical methods. *Near Surface Geophysics*, 18, 217–248. https://doi.org/10.1002/nsg.12097

Sirgue, L., & Pratt, R. G. (2004). Efficient waveform inversion and imaging: A strategy for selecting temporal frequencies. *Geophysics*, 69, 231–248. https://doi.org/10.1190/1.1649391

Sporn, K., Andonova, M., Biernath, S., Bilis, T., Czysz, W., Dogani, I., ... Zipprich, S. (2017). Forschungen zur Anlage, Ausdehnung und Infrastruktur des Heiligtums von Kalapodi. *Mitteilungen des Deutschen Archäologischen Instituts - Athenische Abteilung*, 131/132, 193–278.

Tanner, A. (2019). *Three Hellenistic 'Naïskoi' in the Theatre Area at Aigeira: Small buildings in the context of an urban sanctuary* (pp. 74–87). Brill.

Tran, K. T., McVay, M., Faraone, M., & Horhota, D. (2013). Sinkhole detection using 2D full seismic waveform tomography. *Geophysics*, 78, R175–R183. https://doi.org/10.1190/geo2013-0063.1

Trinks, I., Hinterleitner, A., Neubauer, W., Nau, E., Löcker, K., Wallner, M., ... Seren, S. (2018). Large-area high-resolution ground-penetrating radar measurements for archaeological prospection. *Archaeological Prospection*, 25, 171–195. https://doi.org/10.1002/arp.1599

Ulugergerli, E. U., & Uyanik, O. (2007). Statistical correlations between seismic wave velocities and SPT blow counts and the relative density of soils. *Journal of Testing and Evaluation*, 35, 187–191.

Vafidis, A., Manakou, M., Kritikakis, G., Voganatsis, D., Sarris, A., & Kalpaxis, T. (2003). Mapping the ancient port at the archaeological site of Itanos (Greece) using shallow seismic methods. *Archaeological Prospection*, 10, 163–173. https://doi.org/10.1002/arp.212

Virieux, J., & Operto, S. (2009). An overview of full- waveform inversion in exploration geophysics. *Geophysics*, 74, WCC1–WCC26. https://doi.org/10.1190/1.3238367

Wilken, D., Köhn, D., Schwardt, M., Wunderlich, T., Rabbel, W., Werther, L., ... and Brückner, H. (2019) Can seismic resolution match coring and excavation data? Full waveform inversion in archaeological prospection. In AGU Fall Meeting Abstracts, vol. *2019*.

Wilken, D., Wunderlich, T., Stümpel, H., Rabbel, W., Pašteka, R., Erkul, E., ... Kušnirák, D. (2015). Case history: Integrated geophysical survey at Katarínka monastery (Slovakia). *Near Surface Geophysics*, 13, 585–599. https://doi.org/10.3997/1873-0604.2015027

Woelz, S., Rabbel, W., & Mueller, C. (2009). Shear waves in near surface 3D media-SH-wavefield separation, refraction time migration and tomography. *Journal of Applied Geophysics*, 68, 104–116. http://eprints.uni-kiel.de/9844/

Wu, R. S., & Toksöz, M. N. (1987). Diffraction tomography and multisource holography applied to seismic imaging. *Geophysics*, 52, 11–25. https://doi.org/10.1190/1.1442237

Wunderlich, T., Wilken, D., Erkul, E., Rabbel, W., Vött, A., Fischer, P., ... Heinzelmann, M. (2018). The river harbour of Ostia Antica—Stratigraphy, extent and harbour infrastructure from combined geophysical measurements and drillings. *Quaternary International*, 473(1238), 55–65. https://doi.org/10.1016/j.quaint.2017.07.017

APPENDIX A.

TABLE A1 Methods and processing of measurements preceding this study (cf. Figure 2)

Equipment	Configuration	Processing
Magnetic mapping		
6 × Fluxgate gradiometer Type: Foerster Ferex 650	*dx*: 0.5 m	Subtraction of mean of each profile
	dy: 20 Hz = ∼0.05 m	
GPR		
400-MHz antenna and SIR30 registration unit both by GSSI	*dx*: 0.3 m	T0 correction
	dy: 50 scans per second	Georeferencing
	T: 50 ns	Binning: 0.02-m trace spacing
		Horizontal and inline offset removal
		Finite difference migration with linear 1D gradient
		Dipfilter (−1, 0.7, 0.7, 1)
ERT		
RESECS registration unit and cables by Geoserve	*dx* and *dy*: 1 m	Assign coordinates and topography to electrodes
	Dipole–dipole	Inversion with BERT
	Wenner-beta	Size of cells at surface: 0.2 m
		Jacobian matrix is recalculated in every iteration
		Regularization strength $\lambda = 10$
		Robust and blocky model = L1 norm
		Vertical constrains weight = 1

Abbreviations: BERT, boundless electrical resistivity tomography (Günther et al., 2006; Rücker et al., 2006); *dx*, profile spacing; *dy*, inline spacing (sampling rate, scan rate and electrode spacing); ERT, electrical resistivity tomography; GPR, ground-penetrating radar.

TABLE A2 Parameters and properties used for the FWI

Step	Parameter	
Model discretization	Grid points in *x*	1024
	Grid points in *y*	288
	Grid spacing	0.025 m
	Time step	8×10^{-6}
Initial model	Shear-wave velocity	Smoothed first arrival result (gauss taper: 20 points)
	Density	$\rho = 1000 \cdot (0.1055 \cdot \log(vs) + 1.3871)$ after Ulugergerli and Uyanik (2007)
	Q_s	Half-space: 60, 30, 15
Inversion steps	Low-pass	80, 90, 100, 170, 120, 130, 170, 200, 230, 260 and 300 Hz
	Band-pass	80–300, 150–300 and 250–300 Hz
	Low-pass	300 Hz
Boundaries	Surface	Free surface
	Other	PML 10 grid points (2.5 m)

Abbreviations: FWI, full-waveform inversion; PML, perfectly matched boundary; Q_s, shear-wave velocity quality factor.
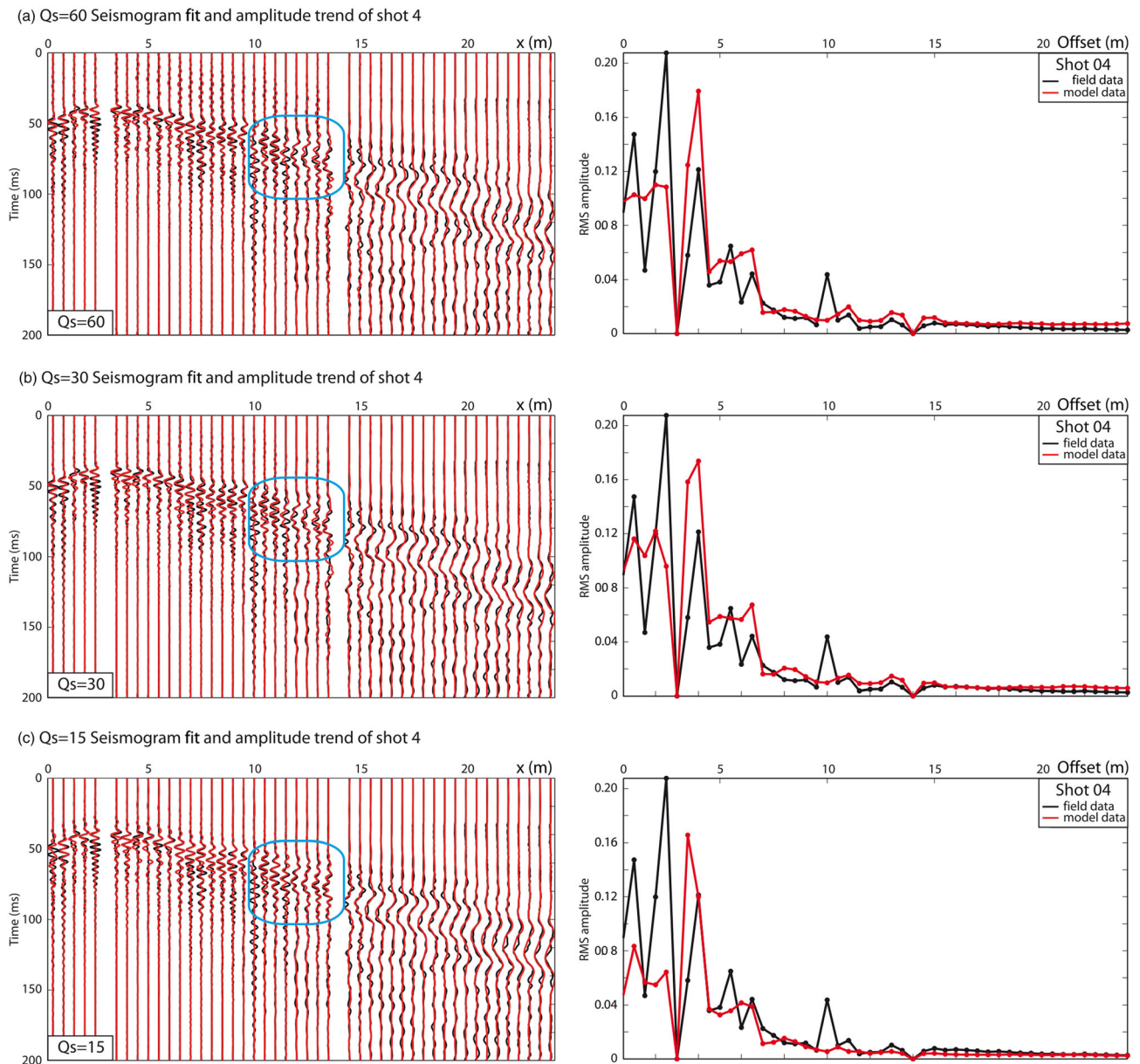
FIGURE A1 Comparison of seismogram and amplitude trend fits for different Q_s values. (a) $Q_s = 60$. (b) $Q_s = 30$ improves the fit. (c) $Q_s = 15$ shows the best fit [Colour figure can be viewed at wileyonlinelibrary.com]
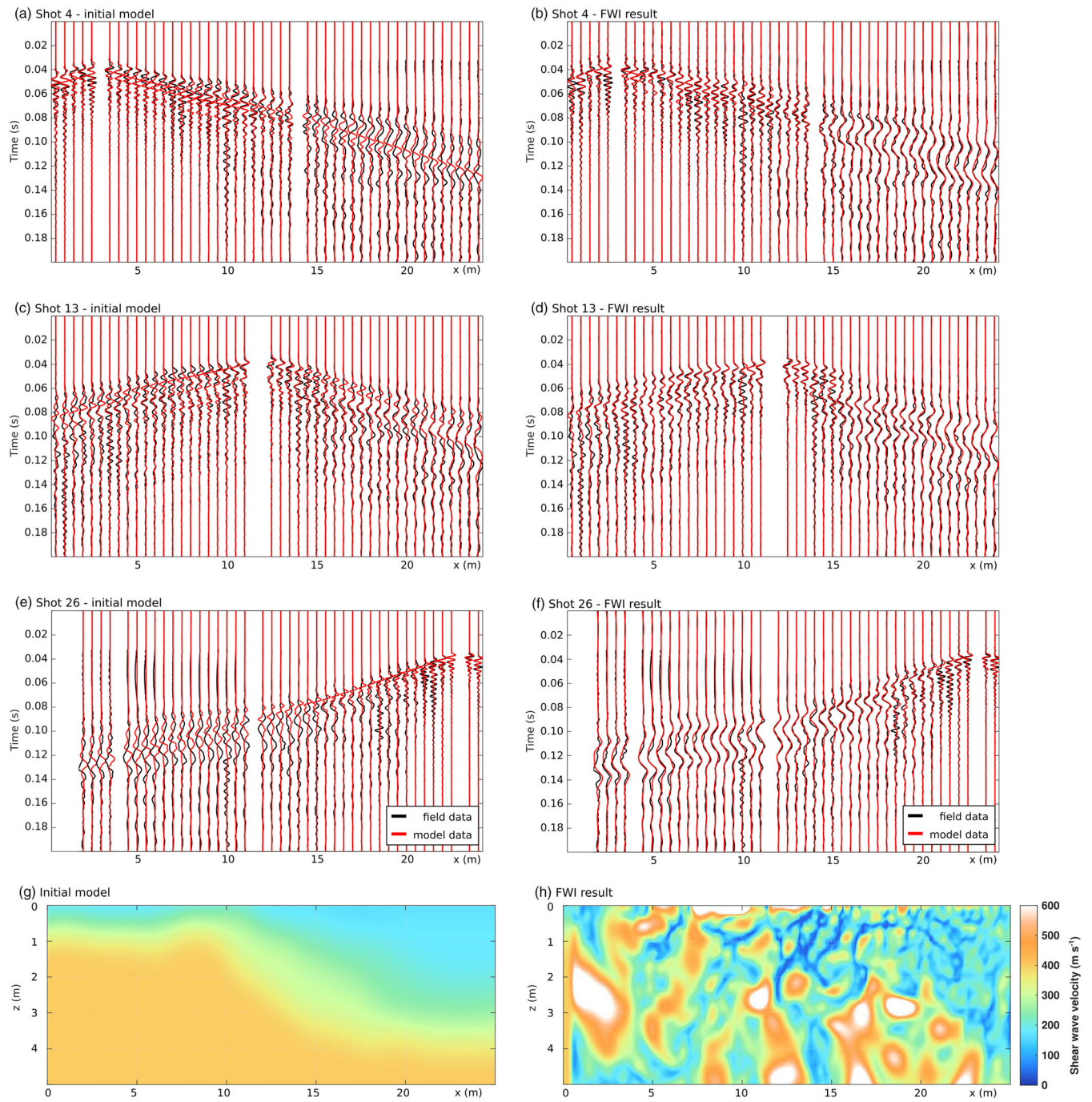
FIGURE A2 Comparison of measured data and synthetic seismograms of (a,c,e) the initial model and (b,d,f) the full-waveform inversion (FWI) result model. The used shear-wave velocity models of (g) the initial model and (h) the FWI result are shown as well [Colour figure can be viewed at wileyonlinelibrary.com]
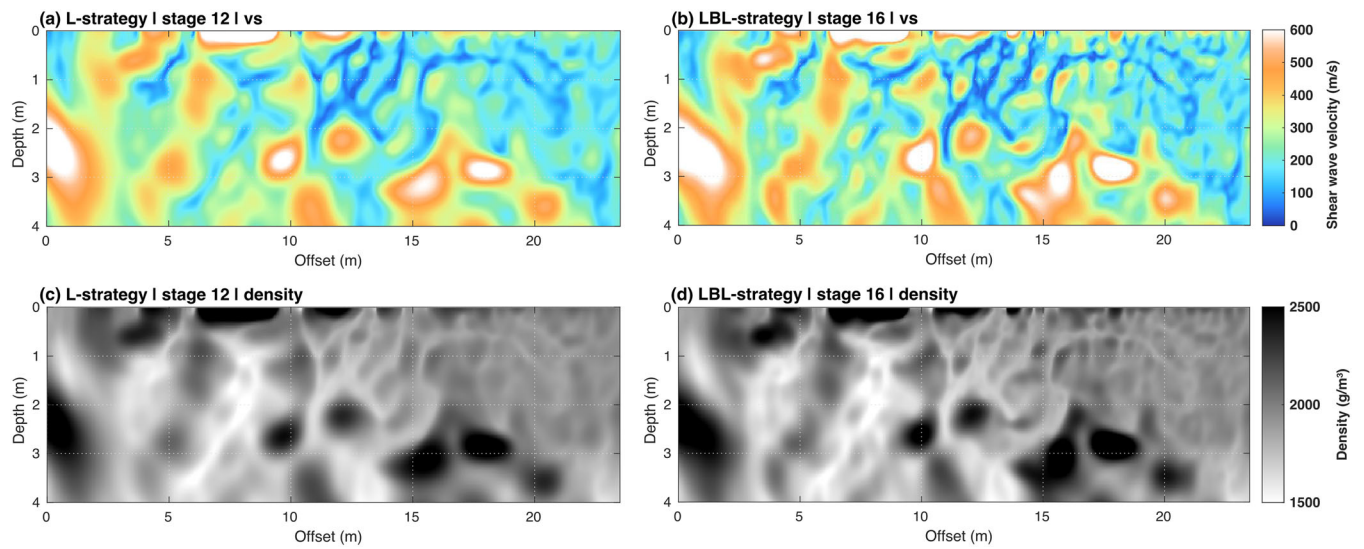
FIGURE A3 Comparison of different full-waveform inversion (FWI) strategies. L strategy only uses low-pass filtered data (see Table A2) whereas the LBL strategy adds additional band-pass and another low-pass stages on top of the L result. Shown are the results for the shear-wave velocity (a, L strategy; b, LBL strategy) and for the density (c, L strategy; d, LBL strategy) [Colour figure can be viewed at wileyonlinelibrary.com]